


ORIGINAL ARTICLE

Hippocampal hyperactivity in a rat model of Alzheimer's disease

Liudmila Sosulina^{1,2} | Manuel Mittag³  | Hans-Rüdiger Geis¹ | Kerstin Hoffmann³ | Igor Klyubin⁴ | Yingjie Qi⁴ | Julia Steffen³ | Detlef Friedrichs¹ | Niklas Henneberg¹ | Falko Fuhrmann¹ | Daniel Justus¹ | Kevin Keppler⁵ | A. Claudio Cuello⁶ | Michael J. Rowan⁴ | Martin Fuhrmann³ | Stefan Remy^{1,2}

¹Neuronal Networks Group, German Center for Neurodegenerative Diseases (DZNE), Bonn, Germany

²Department of Cellular Neuroscience, Leibniz Institute for Neurobiology, Magdeburg, Germany

³Neuroimmunology and Imaging Group, German Center for Neurodegenerative Diseases (DZNE), Bonn, Germany

⁴Department of Pharmacology and Therapeutics, Trinity College, Dublin, Ireland

⁵Light Microscopy Facility, German Center for Neurodegenerative Diseases (DZNE), Bonn, Germany

⁶Department of Pharmacology and Therapeutics, McGill University, Montreal, QC, Canada

Correspondence

Martin Fuhrmann, Neuroimmunology and Imaging Group, German Center for Neurodegenerative Diseases (DZNE), Venusberg-Campus 1/99, 53127 Bonn, Germany.
Email: martin.fuhrmann@dzne.de

Stefan Remy, Department of Cellular Neuroscience, Leibniz Institute for Neurobiology, Brennekestraße 6, 39118 Magdeburg, Germany.
Email: stefan.remy@lin-magdeburg.de

Funding information

This work was supported by CoEN/2011/11, the Deutsche Forschungsgemeinschaft (DFG, German Research Foundation—SFB 1089 C01, B06, C05 to MF and SR) and by Science Foundation Ireland, grant no. 14/IA/2571.

Abstract

Neuronal network dysfunction is a hallmark of Alzheimer's disease (AD). However, the underlying pathomechanisms remain unknown. We analyzed the hippocampal micronetwork in transgenic McGill-R-Thy1-APP rats (APPTg) at the beginning of extracellular amyloid beta (A β) deposition. We established two-photon Ca²⁺-imaging in vivo in the hippocampus of rats and found hyperactivity of CA1 neurons. Patch-clamp recordings in brain slices in vitro revealed increased neuronal input resistance and prolonged action potential width in CA1 pyramidal neurons. We did neither observe changes in synaptic inhibition, nor in excitation. Our data support the view that increased intrinsic excitability of CA1 neurons may precede inhibitory dysfunction at an early stage of A β -deposition and disease progression.

KEYWORDS

Alzheimer's disease, disease model, Hippocampus, hyperexcitability, β -amyloidosis

Abbreviations: ACSF, artificial cerebrospinal fluid; AD, Alzheimer's disease; AMPA, alpha-amino-3-hydroxy-5-methyl-4-isoxazolepropionic acid; AP, action potential; APPTg, McGill-R-Thy1-APP rats; A β , amyloid beta; CA, *Cornu Ammonis*; EPSP, excitatory post-synaptic potential; GCaMP6m, genetically encoded calcium indicator 6m; hAPP, human amyloid precursor protein; HWSpr, half-width short-pulse rheobase; IPSP, inhibitory post-synaptic potential; MEA, microelectrode array recordings; PBS, phosphate-buffered saline; PFA, paraformaldehyde; PV, parvalbumin; RMP, resting membrane potential; ROI, region of interest; RT, room temperature; SPR, short-pulse rheobase; WT, wild-type.

Liudmila Sosulina, Manuel Mittag, Martin Fuhrmann and Stefan Remy contributed equally to this work.

Prior submission to the JNC the manuscript was published on BioRxiv: <https://www.biorxiv.org/content/10.1101/2020.06.09.141598v2>

This is an open access article under the terms of the Creative Commons Attribution-NonCommercial-NoDerivs License, which permits use and distribution in any medium, provided the original work is properly cited, the use is non-commercial and no modifications or adaptations are made.

© 2021 The Authors. *Journal of Neurochemistry* published by John Wiley & Sons Ltd on behalf of International Society for Neurochemistry.

1 | INTRODUCTION

Defining the earliest neuronal changes on a cellular and network level of brain organization that precede the clinical manifestation of Alzheimer's disease (AD) remains an important task with potential relevance for early diagnosis, treatment, and prevention. The majority of previous studies that have addressed changes in neuronal integrity and excitability were performed at disease stages, where A β -plaques were reliably detected within the brain region of interest (Bittner et al. 2012; Busche et al. 2008). These studies report changes in the intrinsic excitability, the morphology and the in vivo activity of neurons in the presence of amyloid beta (Busche et al. 2008). Common pathophysiological motifs on the single-cell level were structural alterations such as reduced dendritic arborization, spine loss, synapse loss and reduced cell size (Bittner et al. 2010, 2012; Grutzendler et al. 2007; Le et al. 2001; Moolman et al. 2004; Tsai et al. 2004), which were observed in conjunction with higher neuronal excitability because of altered passive and

active neuronal electrical properties (Siskova et al. 2014). On the circuit level reduced synaptic inhibition has been identified in several rodent models of beta amyloidosis. Inhibitory dysfunction has been associated with the occurrence of aberrant activity patterns such as neuronal hyperactivity (Palop et al. 2007), hypersynchronization within neuronal networks (Iltner et al. 2014; Minkeviciene et al. 2009; Verret et al. 2012) and impaired neuronal oscillations (Iaccarino et al. 2016; Siwek et al. 2015). A current view is that these aberrant forms of neuronal activity are mediated by the action of soluble forms of A β , which shift the balance of excitation and inhibition towards excitation (Palop & Mucke, 2016). Evidence supporting this view are the prevention of neuronal hyperactivity by γ -secretase inhibitors (Busche et al. 2012; Liebscher et al. 2014) and the restoration of physiological activity and oscillatory patterns as well as the amelioration of memory deficits by pharmacological or optogenetic enhancement of inhibition (Bakker et al. 2012; Ambrad Giovannetti & Fuhrmann, 2018; Sanchez et al. 2012; Schmid et al. 2016). Among the studies that addressed the earliest changes

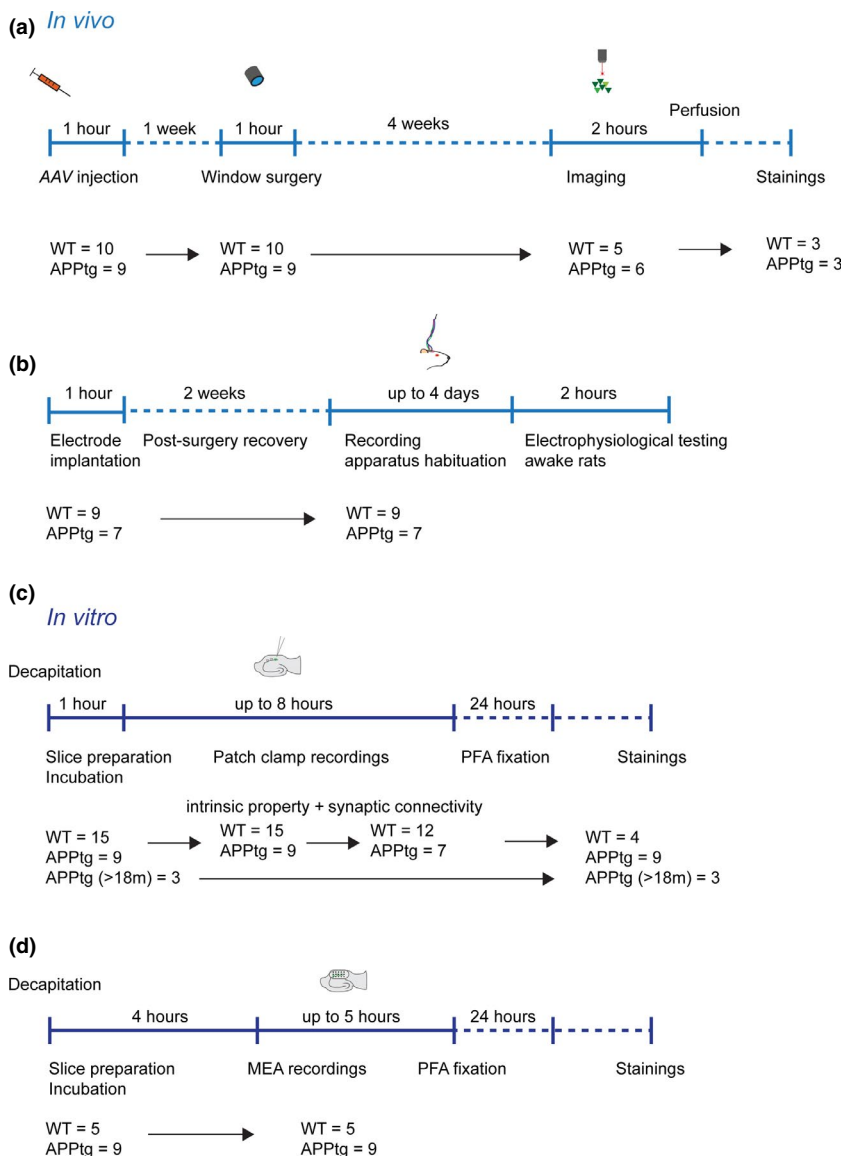


FIGURE 1 Timelines for in vivo (a and b) and in vitro (c and d) experiments described in the manuscript. Numbers below correspond to the animal numbers used for each experimental part



in cellular function at pre-plaque stages the majority report alterations on the synaptic level including synaptic plasticity (Mucke & Selkoe, 2012; Qi et al. 2014; Rowan et al. 2003), but evidence for neuronal hyperactivity within the hippocampus has also been provided (Bezzina et al. 2015; Brown et al. 2011; Busche et al. 2012; Kazim et al. 2017). Here, we investigated whether intrinsic neuronal excitability changes and inhibitory circuit dysfunction are mechanistically involved in neuronal hyperactivity within the CA1 hippocampal subfield at an early stage of extracellular A β deposition. We used transgenic McGill-R-Thy1-APP rats (APPTg), a model with AD-like pathology over-expressing hAPP (human amyloid precursor protein) that exhibits a slow progression of amyloidosis, synaptic, and memory deficits (Leon et al. 2010; Qi et al. 2014).

2 | MATERIALS AND METHODS

2.1 | Animals

Transgenic rats expressing human APP₇₅₁ with Swedish (APP_{KM670/671NI}) and Indiana (APP_{V717V}) mutations under the control of the murine Thy1.2 promoter (McGill-R-Thy1-APP) (Leon et al. 2010) of both genders were investigated. In this study, we used 6- to 9-month-old homozygous McGill-R-Thy1-APP rats (APPTg) and compared them with wild-type (WT) littermates. In this study, in total we used 42 WT rats and 37 APPTg rats (Figure 1). This number corresponds to the original number of used animals. As previously published, homozygous APPTg rats displayed a behavioral phenotype as early as 3 months of age in the Morris water maze task (Galeano et al. 2014; Petrusek et al. 2018) and in a visual discrimination task at the age of 4–6 months (Wilson et al. 2017). Furthermore, at the age of 7–10 months APPTg displayed altered profiles of social behavior and ultrasonic communication as well as increased locomotor activity during active periods of the circadian cycle (Petrusek et al. 2018). To obtain homozygous APPTg and WT rats, we crossed heterozygous APPTg rats and identified homozygosity using a qPCR protocol. Furthermore, we carried out backcrossing with WT rats for one generation in some cases. McGill-R-Thy1-APP rats were genotyped as described previously (Galeano et al. 2014; Leon et al. 2010). Briefly, genomic DNA was isolated from ear punches, using the peqGOLD Tissue DNA Mini Kit S-Line (PEQLAB Biotechnologie, Erlangen, Germany, cat.no. 12-3396-xx). The DNA concentration was measured by Peqlab NANODROP2000c (PEQLAB Biotechnologie, Erlangen, Germany, cat.no. NANODROP-2000). For distinguishing between homo- und heterozygous McGill-R-Thy1-APP rats qPCR was performed using the following primers: human APP-specific primers (forward: 5' ATCCCACTCGCACACAGCAG3', reverse: 5'GGAATCACAAAGTGGGGATG3') and GAPDH (forward: 5'GGGGAAGGACGCTGTACGGG3', reverse 5'AAGGGGAGCAACAGCTGGGGT3'). For qPCR each sample was processed three times in two dilutions with a total of 7 ng and 14 ng of genomic DNA. The standard curve was determined on Applied Biosystems 7900HT Fast Real-Time PCR System (Applied

Biosystems, cat.no. 4329001) using 2 x PowerSYBR Green PCR Master Mix (Applied Biosystems, cat.no. 4368577). The quantification was performed using $2^{-\Delta\Delta Ct}$ method and at least one sample of known heterozygous genotype served as internal standard. For the calcium imaging experiment, the wild-type group was consisting of four male and one female animals. The homozygous group was consisting of four male and two female animals. For the in vitro electrophysiology and stainings 17 WT female rats and three male rats, as well as 13 transgenic females and eight transgenic males have been used. The weight of the female animals was ranging from 280 to 400 g, whereas the weight of the male rats was between 550 and 650 g. The animals were housed in cages (1290D Eurostandard typ 3 with elevated grid cover, Techniplast, Varese, Italy) containing one to two animals with 12-to-12 hr-light-dark cycle. All experiments were performed in the light phase of the circle. The timelines of in vivo and in vitro experiments are summarized in Figure 1, Food and water were provided ad libitum. All experiments were performed in agreement with European Committees Council Directive (RL2010/63/EU) and were approved by the local authorities Landesamt für Natur, Umwelt und Verbraucherschutz (LANUV) of North Rhine-Westphalia (Az84-02.04.2012.A371).

2.2 | Slice preparation

Horizontal hippocampal slices were prepared as described previously (Fuhrmann et al. 2015). In brief, rats were anesthetized with ketamine (0.13 mg/g, Ketamin 10%, Medistar GmbH, Ascheberg, Germany) and xylazine (0.01 mg/g, Rompun 2%, Bayer, Leverkusen, Germany) before being decapitated. The brains were quickly transferred to ice-cold sucrose solution, containing the following components in mM: 60 NaCl, 100 sucrose, 2.5 KCl, 1.25 NaH₂PO₄, 26 NaHCO₃, 1 CaCl₂, 5 MgCl₂, 20 glucose, oxygenated with 95% O₂ and 5% CO₂. Horizontal hippocampal slices (300 μ m thickness) were prepared on a VT-1200S vibratome (Leica Microsystems, Wetzlar, Germany) and transferred to a submerged chamber at 35°C for 30 min and kept at 20–22°C thereafter in standard ACSF solution, containing in mM: 125 NaCl, 3 KCl, 1.25 NaH₂PO₄, 26 NaHCO₃, 2.6 CaCl₂, 1.3 MgCl₂, 15 glucose.

2.3 | Whole-cell patch-clamp recordings

Current-clamp recordings were performed using an BVC-700A amplifier (Dagan) with standard ACSF solution at 34°C containing the GABAB-receptor blocker CGP55845 (1 μ M, Tocris, cat.no. 1248). Recording pipettes with a resistance of 3–5 M Ω were pulled with a DMZ universal electrode puller (Zeitz-Instruments Vertriebs-GmbH, Martinsried, Germany) and filled with intracellular solution of the following composition in mM: 140 K-gluconate, 7 KCl, 5 HEPES-acid, 0.5 MgCl₂, 5 phosphocreatine, 0.16 EGTA. The liquid junction potential of –10 mV was not corrected. Signals were digitized at \geq 25 kHz using an ITC-18 interface board controlled by custom-written

procedures in Igor Pro (V. 6.31, WaveMetrics Inc.). Resting membrane potential (RMP) was measured immediately after establishing the whole-cell configuration. Following that, the membrane potential was adjusted to -60 mV by continuous current injection. For estimation of the short-pulse rheobase (SPR), short 3 ms current pulses with increasing amplitude in steps of 1 pA were injected until reaching action potential threshold (Siskova et al. 2014). HWspr (half-width short-pulse rheobase) was calculated as the half-width of action potential (AP) duration at the level of 50% of repolarization of the first AP measured with the short-pulse rheobase protocol using the TaroTools (Dr Taro Ishikawa, <https://sites.google.com/site/tarotoolsregister/>) offline routines implemented in Igor Pro (V. 6.31). Hyper- and depolarizing current steps of 1 s duration were applied to calculate the neuronal excitability. Input resistance was calculated from linear fitting the range of current injections (-20 , 0 , 20 and 50 pA) with custom-made Igor Pro software (6.31). HW1 and HW2 represent the duration at half-maximum amplitude of the first and second AP at the maximal current injection of $+500$ pA. Frequency was calculated as the instantaneous frequency between the first two APs following the same current injection. Sag ratio represents the ratio between steady membrane potential and peak potential resulting from a -200 pA current injection.

Recurrent inhibition was studied as described previously (Muller et al. 2012). A cluster electrode (FHC, cat.no. CE2F75) was placed onto the alveus close to the subiculum. Biphasic current pulses were generated using a stimulus isolator (A-M Systems, Model 2100, cat. no. 720000). To isolate CA1 originating recurrent inhibition, the subiculum as well as the CA3 subfield were cut off, sparing the alveus. Input-output curves were created using stimulus durations of 0.15 – 0.2 ms, stepwise increasing intensities by 0.025 mA up to 0.4 mA, using custom-made online routine. Following that, 10 stimulations at theta frequency (5 Hz) were applied, repeated three times and averaged. Additionally, 10 alveus stimulations in 100 Hz bursts at theta frequency (5 Hz) were performed (Muller et al. 2012). Time-curve of IPSP changes was investigated and compared between WT and APPTg McGill rats. For 100 Hz bursts at theta frequency (5 Hz) the first IPSP component of the first pulse was compared with the first IPSP of the last pulse to estimate the contribution of more proximal inhibition. Accordingly, the third IPSP component of 100 Hz burst was compared to the third IPSP component of the last pulse to quantify more distal inhibition.

2.4 | Thioflavin-S staining and determination of plaque load

Acute horizontal hippocampal slices of 300 μ m thickness were fixed for 24 hr in PFA (4%) and washed two times in 0.1 M PBS. The slices were preserved in 0.05% sodium acid in PBS at 4°C before staining. Slices were stained by bath application of 0.1% Thioflavin-S in deionized water for 20 min at RT. A total of four slices from 4 WT rats, nine slices from APPTg rats (6–9 months), used for the patch-clamp experiments, and three slices from old (>18 months) APPTg rats used as a positive control, were stained.

Following the staining, slices were rinsed 3×10 min with PBS to remove the residual dye. Consecutive images through the hippocampus were made with a Zeiss LSM 700 confocal microscope from both sides of the slice using a $10 \times$ objective (Plan-NEOFLUAR $10 \times / 0.3$, Zeiss, Germany, item no. 440330-9902-000). The total number of Thioflavin-S-positive plaques was determined in one hippocampal slice per rat and plaque density was calculated as number of plaques per 1 mm^2 of hippocampal area using ZEN black software (Zeiss, Germany).

2.5 | 6E10 and 4G8 staining and distinguishing between APP and A β

Acute horizontal hippocampal slices of 300 μ m thickness were fixed for 24 hr in PFA (4%) and washed two times in 0.1 M PBS. The slices were permeabilized in 0.5% Triton-X100 in PBS for 1 hr. Then, the slices were incubated overnight in blocking reagent (10% normal goat serum, 1% Triton-X100 and 20% BSA) with primary antibodies—either anti-6E10 ($1:1,000$, Covance, mouse, RRID:AB_662798) and anti-NeuN ($1:1,000$, Covance, rabbit) or anti-4G8 (Covance, mouse, $1:500$, RRID:AB_10175149) and anti-NeuN ($1:1,000$, Covance, rabbit). On the next day, the slices were first washed three times with PBS. The slices were incubated for 1.5 hr in 5% normal goat serum in PBS with secondary antibodies—either anti-mouse Alexa Fluor 488 ($1:400$, ThermoFisher, goat, cat.no. A-11001) and anti-rabbit Alexa Fluor 647 ($1:400$, ThermoFisher, goat, cat.no. A-21244) or anti-mouse Alexa Fluor 405 ($1:400$, ThermoFisher, goat, cat.no. A-3153) and anti-rabbit Alexa Fluor 647 ($1:400$, ThermoFisher, goat, cat.no. A-11001). The slices were washed three times with PBS and mounted with Dako mounting medium (Agilent, cat.no. S302380-2). Fluorescence images of brain section were obtained using a confocal microscope (Zeiss LSM700, Zeiss, Germany).

2.6 | GFAP and Iba1 staining

Three APPTg and three WT rats at the age of 6–9 months and 1–3 months after hippocampal window surgery were injected *intraperitoneally* with $2 \times$ concentrated Ketamine/Xylazine ($0.26/0.02$ mg/g) and then were transcardially perfused using sterile 0.1 M PBS and 4% PFA. The brain was removed and post-fixed in 4% PFA at 4°C overnight. For staining, free-floating coronal hippocampal slices of 50 μ m thickness were produced and incubated overnight in staining solution (4% normal goat serum, 0.4% Triton-X 100 and 4% BSA) with anti-GFAP antibody ($1:1,000$, ThermoFisher, rat, cat.no. 13-0300) and anti-Iba1 antibody ($1:1,000$, Wako, rabbit, cat.no. 019-19741). After washing three times with 0.1 M PBS, the free-floating sections were incubated for 2 hr in staining solution together with anti-rat Alexa 594 and anti-rabbit Alexa 647 ($1:400$, ThermoFisher, goat, cat.no. A-21244). Slices were washed three times with PBS and mounted using Dako Fluorescent mounting medium (Agilent, USA, cat.no. S302380-2). Fluorescence images of brain section were obtained using a confocal microscope (Zeiss LSM700).



2.7 | Microelectrode array (MEA) recordings

For MEA recordings of spontaneous action potentials, hippocampal CA1 slices were prepared the same way as for patch-clamp recordings. After cutting, slices were transferred to an interface chamber (Brain Slice Chamber System with Haas Top, Warner Instruments, Hamden, USA, cat.no. 65-0075) containing ACSF (Maier et al. 2009) for recovery (mM): 119 NaCl, 2.5 KCl, 2.5 CaCl₂, 1.0 NaH₂PO₄, 26 NaHCO₃, 1.3 MgCl₂, 10 glucose, oxygenated with 95% O₂ and 5% CO₂. Inside the interface chamber, hippocampal CA1 slices were kept on lens cleaning tissue (Grade 105, Whatman, Maidenstone, England, cat.no. 2105-841) allowing optimal oxygenation because of a laminar flow of preheated (35°C) ACSF above and underneath the slices for at least 3 hr. The MEAs were positioned in CA1 of dorsal hippocampus. Extracellular waveforms were recorded with a MEA2100-System (Multi Channel Systems, Reutlingen, Germany, RRID:SCR_014809) on 60pMEA100/30iR-Ti MEAs with round titanium nitride (TiN) electrodes. Electrodes were arranged in a 6x10 matrix, with a spacing of 100 µm and an electrode diameter of 30 µm. ACSF temperature was adjusted to 35°C using a heatable perfusion cannula PH01 together with a TC01 controlling unit (Multi Channel Systems, Reutlingen, Germany). A constant negative pressure of 25–30 mBar was applied to the perforated MEAs to stabilize slice position, improve electrode connection, and maintain vertical ACSF flow. Data were sampled at 25 kHz with an MEA2100-lite-Interface Board and acquired with MC_Rack (V 4.5.16.0, Multi Channel Systems, Reutlingen, Germany).

Ten-minutes MEA recording epochs were analyzed using the open-access template-based unit-detection and -sorting algorithm Kilosort (Stringer et al. 2016) (<https://github.com/cortex-lab/KiloSort>) in Matlab (MathWorks, R2016a). The following parameters were used for the spike sorting:

```
ops.Nfilt = 256; ops.whitening = 'full'; ops.nSkipCov = 1;
ops.whiteningRange = 32; ops.criterionNoiseChannels = 0.2;
ops.Nrank = 3; ops.nfullpasses = 6; ops.maxFR = 20,000; ops.
fshigh = 500; ops.fslow = 2000; ops.ntbuff = 64; ops.scale-
proc = 200; ops.NT = 32*1,024 + ops.ntbuff; ops.Th = [2 8 8]; ops.
lam = [5 20 20]; ops.nannealpasses = 4; ops.momentum = 1./[20
400]; ops.shuffle_clusters = 1; ops.mergeT = 0.1; ops.splitT = 0.1;
ops.initialize = 'fromData'; ops.spkTh = -5; ops.loc_range = [3 1];
ops.long_range = [30 6]; ops.maskMaxChannels = 5; ops.crit = 0.65;
ops.nFiltMax = 10,000.
```

Automatically detected units were manually validated using Phi (Rossant et al. 2016). For an identified unit, the mean waveform was calculated from 2000 random spikes events corresponding to this unit. Half-width of the extracellular spikes was determined at the half-maximum of the mean spike waveform negative deflection.

2.8 | Data analysis

Analysis of calcium fluorescence signal was performed using custom analysis software routines in Fiji and Igor Pro. Motion correction of calcium time series was performed using the batch registration

function of the custom Fiji macro TurboReg (Dr Philippe Thévenaz, Swiss Federal Institute of Technology).

Cells were manually identified from the maximum intensity projection of single-trial time series and marked as region of interest (ROI) using Fiji. Change in calcium intensity over time was obtained for every ROI. Calcium signals were depicted as relative fluorescence change, $\Delta F/F$. The $\Delta F/F$ was calculated by subtracting the baseline fluorescence F_0 from the signal and dividing the value by F_0 , $\Delta F/F = (F - F_0)/F_0$. F_0 was defined as the mean of the smallest 40% of all values in a time series. For further analysis, we used the custom macro Taro Tools (Dr Taro Ishikawa, <https://sites.google.com/site/tarotoolsregister/>) for Igor Pro (V. 6.20, WaveMetrics Inc., Lake Oswego, USA). The $\Delta F/F$ traces were smoothed using a 5-point, box-smoothing filter. Calcium peaks were identified according to following criteria: First of all, a baseline $\Delta F/F$ for every peak was calculated as the mean of the 5s-window preceding the peak of the event. Calcium events were counted when the peak was three times the SD value of the baseline. Second, the $\Delta F/F$ amplitude of the smoothed calcium event had to be at least 10% since this is the value that has been described as the calcium increase in response to one action potential in the visual cortex (Chen et al. 2013). The third precondition was that two consecutive events had to be separated by at least 500 ms.

Classification of neurons was performed according to previous reports by Busche et al. (Busche et al. 2008). The first category, termed "silent cells," comprises neurons that show less than 0.4 Ca²⁺-transients/min. The second category, termed "moderately active cells," represents cells that displayed between 0.4 and 4 Ca²⁺-transients/min. The third category, termed "hyperactive cells" includes all neurons with more than 4 Ca²⁺-transients/min.

Electrophysiological data were recorded and analyzed using Igor Pro (V. 6.31, WaveMetrics). Statistical comparisons were performed with Prism 7 and 8 for Windows (Prism version 7.0.3 and 8.0.2 for Windows, GraphPad Software).

Evoked IPSP was fitted using the function $f(t) = f_0 - A \cdot (1 - \exp(-(t - t_0)/\tau_r))^5 \cdot \exp(-(t - t_0)/\tau_d)$ (Magee & Cook, 2000), where f_0 is a baseline, A is a constant τ_r and τ_d are the rise and decay time constants. IPSP rise and decay time constants were averaged from three repetitive measurements and compared between WT and APPTg. During analysis, the experimenter was unaware of the animal's group.

2.9 | Virus injection

GCaMP6m is a genetically encoded cytoplasmic fluorescent Ca²⁺-indicator that shows high sensitivity and medium decay kinetics compared to GCaMP6s/f (Chen et al. 2013). The K_d value is 164 ± 31 nM, the τ_{on} is 80 ± 7 ms and the τ_{off} is 270 ± 23 ms (Chen et al. 2013). To conditionally express the cytoplasmic fluorescent calcium indicator GCaMP6m with high sensitivity and medium decay kinetics (Chen et al. 2013) in CA1 pyramidal neurons, we anesthetized female and male rats by injecting—either intraperitoneally (i.p.) or intramuscularly (i.m.)—a mixture of Ketamine/Xylazine (0.13/0.01 mg/g). In

this study, we used a combination of ketamine and xylazine for the surgeries to obtain sufficient analgesia and duration of surgical tolerance. This combination is generally accepted for major surgeries in rodents and provides surgery-plane anesthesia and analgesia. When the animal was asleep, we made a small incision using a scalpel and performed a small craniotomy (\varnothing 1 mm) using a dental drill at a previously marked spot overlying the dorsal hippocampus at the coordinates -4.2 mm anterior posterior and $+2.6$ mm mediolateral from bregma. We then injected three times $1\ \mu\text{l}$ ($100\ \text{nl/min}$) of AAV1-*hSyn-GCaMP6m-WPRE* (Addgene, Watertown, USA, cat.no. 100838-AAV1) at each 3.3 mm, 3 mm, and 2.7 mm dorsoventral from the skull surface using a microliter syringe (Hamilton, cat.no. 7635-01) controlled by a four-channel micro controller (SYS-Micro4, World Precision Instruments, USA). After the last injection step, we kept the needle in place for 10 min so that the virus had time to diffuse into the tissue. The needle was carefully removed and the skin was stitched. During surgery, the body temperature of the rats was maintained at a constant level of 37°C using a costume built heating plate. After surgery, the rats were kept separated from housing mates until they were fully awake. Afterwards the animals were treated with Carprofen ($0.05\ \text{mg/kg}$, Rimadyl Injectable, Zoetis, New Jersey, USA, item no. Vet-Rx-MW 026357) two times per day for 3 days.

2.10 | Hippocampal window preparation

The preparation of the cranial window was carried out similar to previously described procedures in mice (Dombeck et al. 2010), including some refinements. The animals were anesthetized by injecting—either i.p. or i.m.—a mixture of Ketamine/Xylazine ($0.13/0.01\ \text{mg/g}$). During the procedure the body temperature was maintained at $\sim 37^\circ\text{C}$ using a heating plate. The eyes of the rat were covered with eye ointment (Bepanthen, Bayer, Leverkusen, Germany) during the surgery. After hair removal with tweezers and disinfecting with 70% ethanol, the skin was opened with a scalpel. The exposed cranial bone was cleaned and dried with Sugi absorbent swabs (Kettenbach GmbH, Germany, cat.no. 30601). The bone surface was scraped and cleaned with a scalpel. For preparing a base-layer of glue to which subsequently all parts of the headholding set were fixed, we used a two-component dental glue (OptiBond FL, cat.no. 26684 E). After drying and roughening of the skull, a thin layer of the priming component was applied for $15\ \text{s}$ to the skull surface with a slight scrubbing motion. The layer was gently air-dried for $5\ \text{s}$. Using the same applicator-brush, a layer of the adhesive component was applied to the skull surface the same way as it was done with the priming component. The glue was then light cured for $20\ \text{s}$. Using a dental drill, we performed a craniotomy (\varnothing 5 mm) around the injection site. Cortical tissue was gently aspirated with a blunt 27 gauge needle until the external capsule became visible. A stainless steel cannula (\varnothing 5 mm, 2.5 mm height) covered with a cover glass (\varnothing 5 mm, 0.17 mm thickness) was inserted into the free space between hippocampus and skull. The small cavity between skull and cannula was sealed with a mixture of dental acrylic cement (Cyano Veneer, Hagerwerken,

Germany, cat.no. 152255) and dental acrylic glue (Cyano Retarder, Hagerwerken, Germany, cat.no. 152262). Using dental cement, a metal headpiece was glued to the skull on the contralateral side in order to allow fixation of the animal under the microscope. After surgery, the rats were kept separated from housing mates until they were fully awake. Afterwards, the animals were treated with Carprofen ($0.05\ \text{mg/kg}$, Rimadyl Injectable, Zoetis, New Jersey, USA, item no. Vet-Rx-MW 026357) two times per day for 3 days.

2.11 | Two-photon calcium imaging

For two-photon imaging we used a TriM Scope II (LaVision BioTec GmbH, Germany) microscope and a $25\times$ 4 mm working-distance, water-immersion objective (numerical aperture = 1, model XLPLN25XSVM2, Olympus). Imaging was performed after ceasing of surgery-induced inflammation response, which in mice takes four weeks (Gu et al. 2014). For excitation of GCaMP6m at $920\ \text{nm}$ we used a standard titanium sapphire (Ti:Sa) laser ($\sim 900\ \text{fs}$ laser pulse width at $80\ \text{MHz}$; Coherent). Fluorescence was assessed using a bandpass filter ($510/20\ \text{nm}$; Semrock, cat.no. FF03-510/20-25). For imaging under anesthesia, the rats were anesthetized with 1% isoflurane in oxygen using an isoflurane vaporizer (Kent Scientific, USA, cat.no. VetFlo-1205S-M) and fixed with the metal bar to a holder in order to allow stable imaging. For imaging, we used a light isoflurane anesthesia to immobilize the rats. Since we did not carry out any invasive procedures during imaging the anesthesia during imaging did not require any additional analgesic substance. During imaging, the body temperature of the rats was maintained at a constant level of 37°C . After imaging, the animals were allowed to fully recover from anesthesia before they were united with housing mates.

2.12 | Electrophysiological recording in freely behaving rats

Recording was carried out in chronically implanted freely behaving 6–9 months old rats. The implantation procedure was carried out under recovery anesthesia using a mixture of ketamine ($80\ \text{mg/kg}$) and xylazine ($8\ \text{mg/kg}$) (both i.p.) according to methods similar to those described previously (Qi et al. 2014). Field EPSPs were recorded from the stratum radiatum in the CA1 area of the dorsal hippocampus in response to stimulation of the ipsilateral Schaffer collateral/commissural pathway. Monopolar recording electrodes ($75\ \mu\text{m}$ inner core diameter, $112\ \mu\text{m}$ external diameter) and twisted bipolar stimulating electrodes ($50\ \mu\text{m}$ inner core diameter, $75\ \mu\text{m}$ external diameter) were constructed from Teflon-coated tungsten wires. The recording site was located $3.8\ \text{mm}$ posterior to bregma and $2.5\ \text{mm}$ lateral to midline, and the stimulating site was located $4.6\ \text{mm}$ posterior to bregma and $3.8\ \text{mm}$ lateral to midline. The final placement of electrodes was optimized by using electrophysiological criteria and confirmed via postmortem analysis. Animals were allowed to recover for at least 2 weeks after implantation surgery



before recording from them as they freely explored a recording box in a well-lit room. The recording box consisted of the base on the home cage, including normal bedding and food/water, with the sides replaced with translucent Perspex walls (27 x 22 x 30 cm) and an open roof. The rats had access to food and water throughout the whole recording session from the same position as in the home cage. All animals were first habituated to the recording procedure over the post-surgery recovery period. Test EPSPs were evoked by square wave pulses (0.2 ms duration) at a frequency of 0.033 Hz and an intensity that triggered a 50% maximum response as determined after constructing an input-output curve.

2.13 | Study design

At the start of the study, no sample calculation was performed. No pre-specific primary or secondary endpoints were set. The study was explanatory. At the start of the study, no specific inclusion or exclusion criteria were pre-determined.

3 | RESULTS

3.1 | Increased Ca^{2+} -transient frequency of hippocampal CA1 pyramidal neurons

Hyperactivity of neurons in the cortex and hippocampus of mice has been previously shown to occur in proximity of A β -plaque depositions (Busche et al. 2008) and at pre-plaque stage (Busche et al. 2012). Therefore, we first addressed, whether hyperactive neurons are equally present at an early stage of A β -plaque deposition in the hippocampus of our transgenic rat model. We used homozygous Thy1-APP-tg (APPtg) and non-transgenic wild-type (WT) rats. We established a cranial hippocampal window that enabled us to carry out two-photon in vivo imaging in rats (Figure S1, online resource). We built a headpiece that was permanently attached to the skull with dental acrylic (Figure S1a, online resource). A headbar served as temporary adapter to attach the rat in anesthesia to the in vivo headpost stand (Figure S1b and c, online resource; see Material and Methods). Since microgliosis and reactive astrocytes have been shown to be associated with hippocampal window implantation (Gu et al. 2014), we investigated both parameters (Figure S1d, online resource). We found that the number of microglia were not different between the implanted and non-implanted hemispheres of APPtg and WT rats (Figure S1e and f, online resource). While the number of astrocytes were decreased on the ipsilateral side in WT rats, the number of astrocytes was comparable between ipsi- and contralateral hemisphere of APPtg rats and the contralateral hemisphere of WT rats (Figure S1g, h, online resource). These results indicated that inflammation on the ipsilateral side decayed to levels of the contralateral side at least 3 weeks after surgery in both APPtg and WT rats. This is in line with previous results obtained in mice (Gu et al. 2014). Previous studies on our transgenic rat model found a

start of A β -plaque deposition in the hippocampus at 6–9 months of age (Hegglund et al. 2015; Leon et al. 2010; Qi et al. 2014). In order to confirm this result, we analyzed extracellular A β -plaques within our experimental groups at 6–9 months of age. To discriminate between different A β -plaque aggregation stages and intracellular APP, we used different antibodies. The 6E10 antibody was used to detect extracellular A β in aged APPtg rats (Figure S2a; lower panel: >18-month APPtg). Furthermore, since 6E10 also detects APP, we were able to stain for intracellular APP accumulation in CA1 neurons of 6- to 9-month-old APPtg, but not WT rats (Figure S2a; middle panels: 6- to 9-month APPtg vs. upper panel 6- to 9-month WT). Using the 4G8 antibody that detects A β , but not APP, we identified no A β -plaques in 6- to 9-month-old WT, a few A β -plaques in 6- to 9-month-old APPtg and many A β -plaques in >18-month old APPtg rats (Figure S2b). Furthermore, to detect fibrillar A β -plaques, we also carried out a Thioflavin S staining. At 6–9 months, we only detected a few fibrillary A β -plaques in the hippocampus of APPtg rats (Figure S2, online resource). In contrast, Thioflavin-S-positive A β -plaques were strongly increased in APPtg rats older than 18 months of age (Figure S2f, online resource). These data indicate that although APPtg rats already exhibited intracellular APP overexpression at 6–9 months of age, only a few extracellular A β -plaques were present at this age in the hippocampus.

In order to assess if chronic hippocampal windows in the rat allowed for robust recording of Ca^{2+} -transients in populations of CA1 neurons we injected a recombinant adeno-associated virus encoding the genetically encoded Ca^{2+} -indicator GCaMP6m driven by a synapsin promoter (*rAAV-hSyn-GCaMP6m*). Next, we performed two-photon in vivo imaging of GCaMP6m expressing CA1 neurons in isoflurane (1%) anesthesia (Figure 2a and b). APPtg rats exhibited significantly more Ca^{2+} -transients per neuron than WT rats (Figure 2b). In total, we monitored 1623 neurons in WT rats (WT, 6–9 months old, 31 imaging areas in 5 animals) and 2051 neurons in APPtg rats (APPtg, 6–9 months old, 35 imaging areas in 6 animals). We monitored the occurrence of spontaneous somatic Ca^{2+} -transients as an indicator of neuronal activity. First, we detected a prominent shift in CA1 neurons toward higher frequencies of Ca^{2+} -events in APPtg compared to WT rats (Figure 2c). We further assessed CA1 network activity by determining the proportion of active neurons that exhibited at least one Ca^{2+} -transient throughout the 2-min recording (Figure 2d). Furthermore, we calculated the mean Ca^{2+} -transient frequency (Figure 2e). We found that the proportion of active CA1 neurons and their mean Ca^{2+} -transient frequency was significantly increased in APPtg compared with WT rats (APPtg: 69.63 [56.06; 80.21] % vs. WT: 30.21 [7.83; 55.26] %; APPtg: 6.51 [2.46; 8.41] min^{-1} versus. WT: 0.60 [0.14; 1.41] min^{-1}). In order to further specify this finding, we classified the cells into categories of silent, moderately active and hyperactive neurons according to previous reports (Busche et al. 2008, 2012). In WT rats (Figure 2f) the majority (>95%) of CA1 neurons were either categorized as silent (61%) or moderately active (36%). Hyperactive neurons only made up for a marginal proportion (3%). On the other hand, in APPtg rats the proportions were strongly shifted (Figure 2g). Hyperactive CA1 neurons formed the largest population (38%),

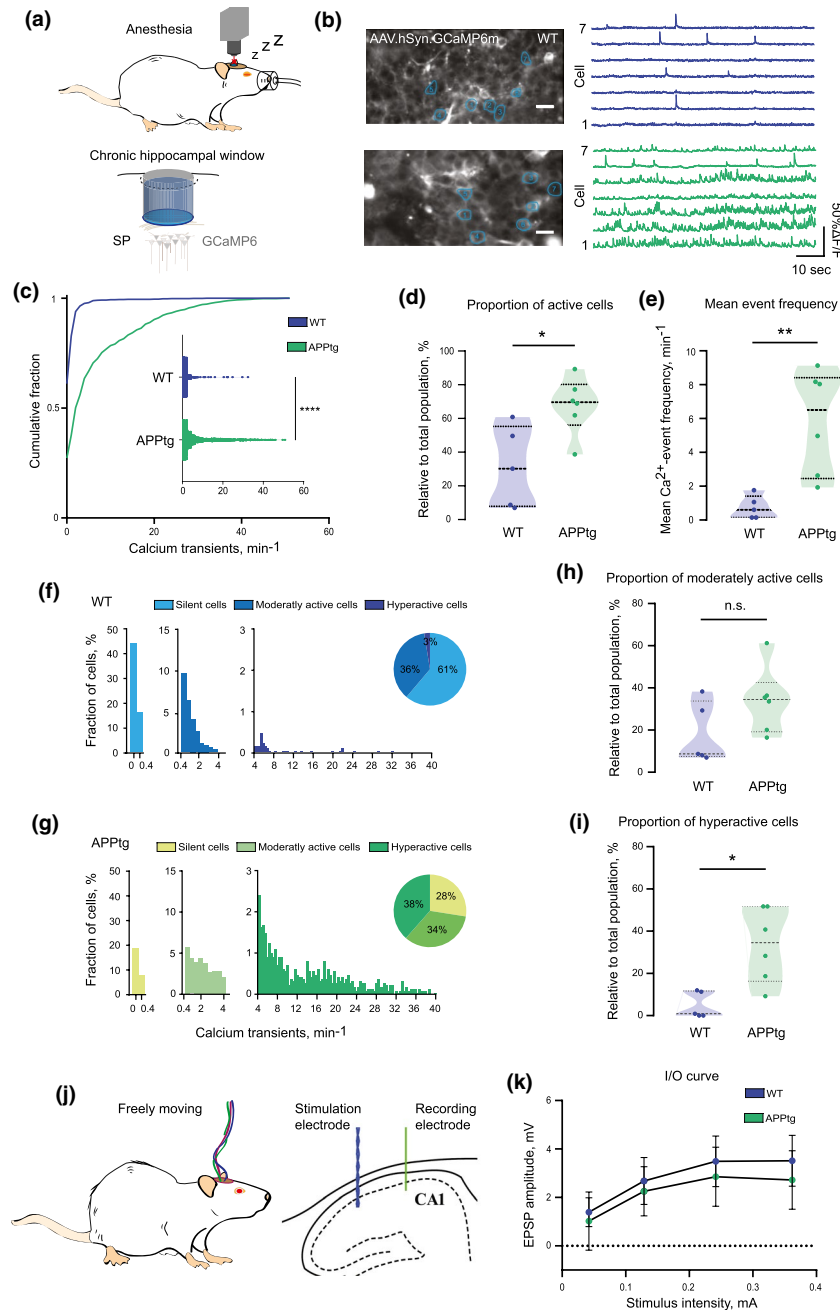


FIGURE 2 Imaging of CA1 neurons in the dorsal hippocampus of APPtg rats. (a) Schematic illustration of a chronic cranial window in rats that allows imaging of neurons in stratum pyramidale (SP) in the CA1 region of the dorsal hippocampus. (b) Exemplary picture of CA1 neurons and respective calcium traces in WT and APPtg rats. (c) Cumulative density plot of pooled cells of WT ($n = 1623$) and of APPtg ($n = 2051$) comparing calcium event frequencies (Kolmogorov–Smirnov test, **** $p < 0.0001$, $D = 0.468$). (d) Comparison of Proportion of active cells (cells that show at least one Ca²⁺-transient during recording time) in WT rats ($n = 5$, 30.21 [7.83; 55.26] %) and APPtg rats ($n = 6$, 69.63 [56.06; 80.21] %) averaged over animals (Mann–Whitney test, $p = 0.017$). Values are displayed as median [25% Percentile; 75% Percentile]. (e) Comparison of mean Ca²⁺-transient frequency in WT rats ($n = 5$, 0.60 [0.14; 1.41] min⁻¹) and APPtg rats ($n = 6$, 6.51 [2.46; 8.41] min⁻¹) averaged over rats (Mann–Whitney test, $p = 0.004$). (f) Pooled cells from all WT rats categorized into silent cells (<0.4 Ca²⁺-transients/min), moderately active cells (0.4–4 Ca²⁺-transients/min) and hyperactive cells (>4 Ca²⁺-transients/min). (g) Pooled cells from all APPtg rats categorized into silent cells, moderately active cells and hyperactive cells. (h) Comparison of moderately active cells (0.4–4 Ca²⁺-transients/min) in WT rats ($n = 5$, 8.72 [7.48; 33.79] %) and APPtg rats ($n = 6$, 34.49 [19.16; 42.59] %) averaged over animals (Mann–Whitney test, $p = 0.178$). (i) Comparison of hyperactive cells (>4 Ca²⁺-transients/min) in WT rats ($n = 5$, 0.92 [0; 11.66] %) and APPtg rats ($n = 6$, 34.53 [16.29; 51.71] %) averaged over animals (Mann–Whitney test, $p = 0.017$). (j) Schema of recording (green) and stimulation (blue) electrode configuration in the area of CA1 of the dorsal hippocampus of freely behaving rat. (k) Baseline synaptic efficacy, as measured by the electrically evoked field EPSP input-output curve, was not different between WT and APPtg rats (Two-way RM ANOVA). Values are displayed as mean \pm SD. Scale bars = 20 μm

exceeding the moderately active population (34%) and the silent population (28%). Comparing the proportions of moderately active and hyperactive CA1 neurons between WT and APPtg rats revealed no change in the population with moderately active neurons (Figure 2h; WT: 8.72 [7.48; 33.79] % vs. APPtg: 34.49 [19.16; 42.59] %). On the other hand, the proportion of hyperactive CA1 neurons was significantly increased in APPtg compared to WT rats (Figure 2i; APPtg: 34.53 [16.29; 51.71] % vs. WT: 0.92 [0; 11.66]). These results show an increased fraction of hyperactive neurons in dorsal CA1 of APPtg rats. In order to determine whether an increase in glutamatergic synaptic transmission contributed to the observed CA1 pyramidal neuron hyperactivity, we measured hippocampal electrically evoked synaptic input–output relationships in a freely-behaving rats. Similar to our findings in younger animals (Qi et al. 2014), baseline transmission at CA3 to CA1 synapses was statistically indistinguishable between 6- and 9-month-old WT and APPtg rats (Figure 2k). These results do not support a role for increased glutamatergic synaptic transmission as a cause of the neuronal hyperactivity in the CA1 area of APPtg rats.

3.2 | Intact parameters of inhibitory neurotransmission in CA1 of APPtg rats

Previous studies in mouse models of AD revealed deficits on the level of synaptic inhibition that contributed to neuronal network dysfunction and were thought to underlie learning and memory impairments (Hamm et al. 2017; Hollnagel et al. 2019; Schmid et al. 2016; Verret et al. 2012). Therefore, we tested whether APPtg rats also exhibited impaired inhibition (Leon et al. 2010; Qi et al. 2014). We carried out alveus stimulation in brain slices *in vitro* in order to recruit full recurrent inhibition and to further dissect the proximal and distal dendritic inhibitory component according to established paradigms (Muller et al. 2012; Pouille & Scanziani, 2004) (Figure 3). With increasing stimulation intensity, we did not observe differences between the input–output curves of WT and APPtg rats (Figure 3a and b). In agreement with these finding, the maximal IPSP amplitude remained unchanged (WT: -4.57 ± 1.39 mV; APPtg: -3.83 ± 1.49 mV, Figure 3c). We then used 5 Hz stimulation to investigate the frequency-dependent attenuation of IPSPs within the range of physiologically observed theta oscillations (Figure 3d). Moreover, detailed analysis of IPSP kinetics did not reveal differences neither in mean hyperpolarization, nor in IPSP rise and decay time constants between WT and APPtg rats (Figure 3a–c, online resource). No difference in the frequency-dependent dynamics of the IPSP amplitude was observed (Figure 3e; percent reductions 10th versus 1st IPSP: WT 67.80 [54.08; 77.30] % vs. APPtg 69.29 [56.13; 73.82] %). Finally, we applied 100 Hz burst stimulation at theta frequency (5 Hz). This protocol allowed to distinguish the inhibitory circuitry targeting more distal dendrites from proximal inhibition, as a relative reduction in the first intra-burst response predominantly represents proximal inhibition whereas the 3rd intraburst component represents the distal component (Muller et al. 2012; Pouille & Scanziani, 2004) (Figure 3g–h). First, we analyzed the compound

IPSP resulting from three stimulations at 100 Hz burst frequency. The frequency-dependent reduction in IPSP amplitude was unchanged comparing WT and APPtg rats (Figure 3d, online resource) and reached previously described values of 60% (Muller et al. 2012). Furthermore, we analyzed distal and proximal inhibition separately. Reduction of the first component at 100 Hz burst as well as the third component of first pulse in comparison to the last pulse did not deviate between WT and APPtg rats (Figure 3i). These results suggest that neither proximal nor distal inhibition onto CA1 pyramidal neurons is affected in 6- to 9-month-old APPtg rats.

3.3 | Increased intrinsic excitability in APPtg rats

Since the measured inhibitory parameters were intact, we assumed that other mechanisms might be responsible for CA1 neuronal hyperactivity. We have previously shown by using computational modeling on reduced neuronal morphologies of APP/PS1 mice that decreased membrane area was associated with increased neuronal input resistance resulting in increased neuronal excitability (Siskova et al. 2014). We hypothesized that similar as in mice, rats might show increased input resistance. Therefore, we carried out electrophysiological recordings in 15 WT and 9 APPtg rats. We observed a difference in the resting membrane potential between WT and APPtg neurons: APPtg neurons were more depolarized (WT: -61.70 ± 3.457 mV vs. APPtg: -58.67 ± 6.427 mV; Figure 4a). When we injected short step currents (3 ms current with 1 pA increment) CA1 pyramidal neurons in APPtg rats required lower current injections to initiate action potential firing (Short-pulse rheobase of 366.0 [263.3; 523.3] pA in APPtg vs. 503.0 [394.8; 664.5] pA in WT; Figure 4b and c). Moreover, consistent with previous findings in mouse models (Siskova et al. 2014), CA1 pyramidal neurons of APPtg rats had an increased input resistance (by 20%) when compared with WT (92.98 [75.55; 129.2] M Ω m; APPtg: 113.8 [86.22; 147.3] M Ω m; Figure 4d and e). Other electrophysiological parameters, such as firing frequency and after-depolarization (ADP) were not different between the two experimental groups (Figure 4f; Figure S4). The observation that CA1 neurons require less depolarization to discharge is in agreement with our *in vivo* observation of neuronal hyperactivity. It suggests that an elevated intrinsic cellular excitability of CA1 pyramidal cells contributes to neuronal hyperactivity.

3.4 | Increased action potential duration in APPtg rats

We further investigated whether the active properties of CA1 pyramidal neurons differed between the experimental groups. We observed a prolongation of the action potential for short current injections or long current injections at the level of 50% of repolarization (Half-width short-pulse rheobase (HWspr); WT: 0.81 [0.73; 0.94] ms versus. APPtg: 0.91 [0.84; 0.98] ms); Half-width long current injection; WT: 0.83 [0.74; 1.06] ms vs. APPtg: 0.93 [0.86; 1.04] ms;

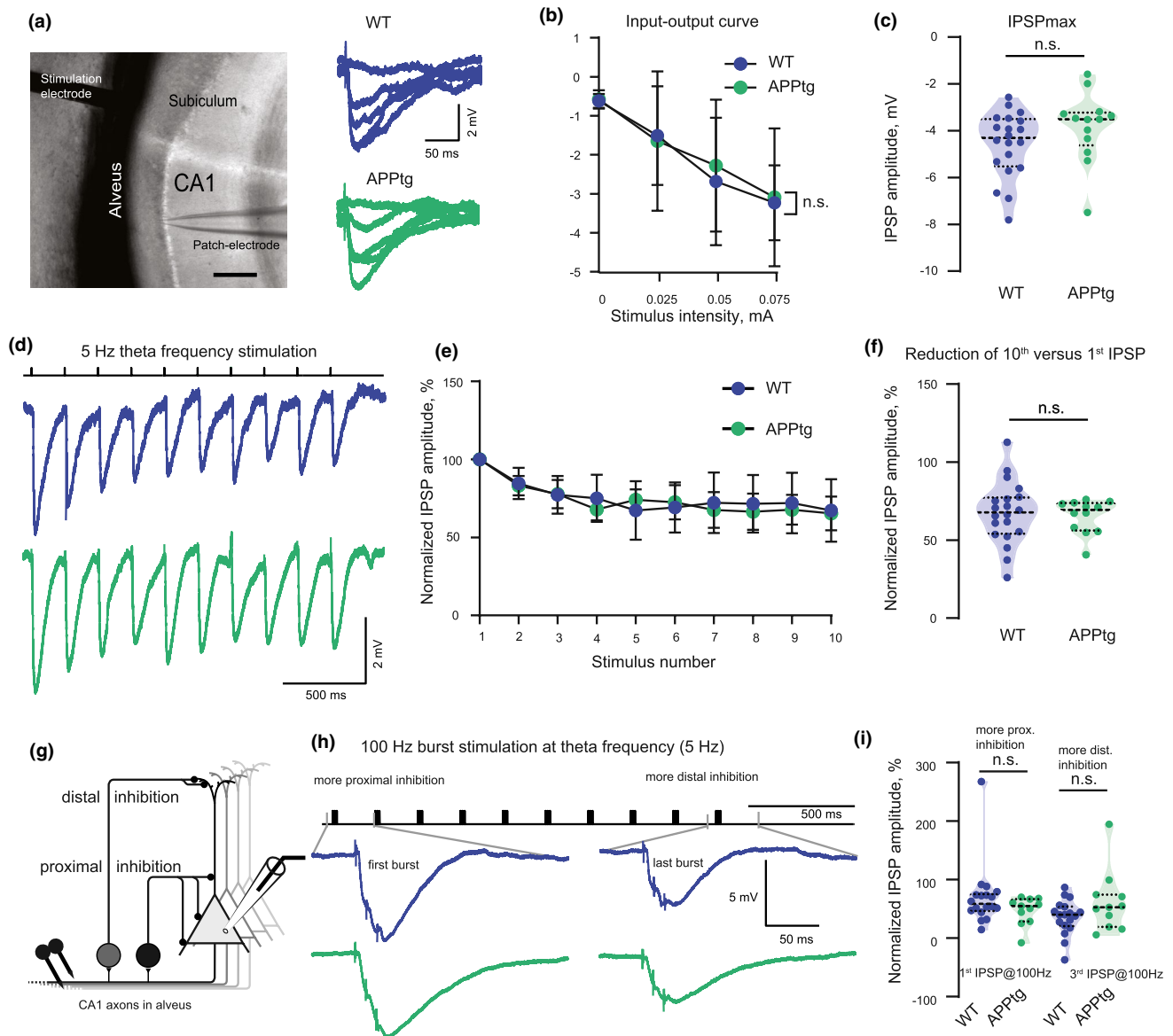


FIGURE 3 Intact proximal and distal inhibition of CA1 neurons in APPtg rats. (a) Experimental setup with stimulation electrode in alveus and patch pipette in CA1 area in rat hippocampal slice. Scale bar, 200 μ m. Representative examples of evoked IPSPs with stimulation intensity increasing from 0 mA to 0.1 mA in 0.025 mA step. Blue lines correspond to WT rats; green to APPtg rats. (b) Extracellular stimulation of a CA1 pyramidal neuron with increasing stimulation intensity of (0, 0.025, 0.05 and 0.075). Input-output relationships were not different between WT and APPtg rats (Two-way RM ANOVA, Sidak's multiple comparisons test). (c) Maximal IPSP amplitudes were not different between WT ($n = 20$ in 12 animals) and APPtg ($n = 13$ in 7 animals) rats (unpaired t -test, $p = .128$). (d) Representative examples of 5 Hz alveus stimulation in WT and APPtg CA1 pyramidal neurons. (e) Normalized IPSP amplitude was not significant different between WT ($n = 20$ in 12 animals) and APPtg ($n = 12$ in 6 animals) rats (Two-way RM ANOVA, Sidak's multiple comparisons test). Error bars represent mean \pm SD. (f) Reduction in IPSP amplitudes 10th (last) versus first stimulation (5 Hz), was not different between WT ($n = 20$ in 12 animals) and APPtg ($n = 12$ in 6 animals) (Mann-Whitney test, $p = .893$). (g) Schematic illustration of alveus stimulation and two types of interneurons targeting more proximal (black) or more distal (gray) dendrites of CA1 pyramidal neuron. (h) Alveus 100 Hz burst stimulation at theta frequency (5 Hz) allows distinguishing proximal and distal inhibition. Lower traces: compound IPSPs in WT and APPtg rats in response to the first compared to the 10th repeated burst. (i) Reduction in the first IPSP amplitudes at 100 Hz burst of the first vs. last stimulation burst (100 Hz burst at 5 Hz), corresponding to more proximal inhibition, was not different between WT ($n = 18$ in 12 animals) and APPtg ($n = 11$ in 6 animals) (Mann-Whitney test, $p = .159$). Reduction in the third IPSP amplitude at 100 Hz burst of the first vs. last burst, corresponding to more distal inhibition, was not different between WT ($n = 18$ in 12 animals) and APPtg ($n = 11$ in 6 animals) (Mann-Whitney test, $p = .238$)

Figure). Finally, we used multi electrode array (MEA) extracellular recordings to confirm our findings obtained in the patch clamp experiments on the population level (Figure 5e-h). The particular advantage of MEA recordings is the undisturbed intracellular milieu of

neurons during the recording. After recording from 60 electrodes in hippocampal slices, we performed spike sorting to identify single units inside the multimodal signal. We compared the duration of the extracellular signal between WT and APPtg rats. Our results further

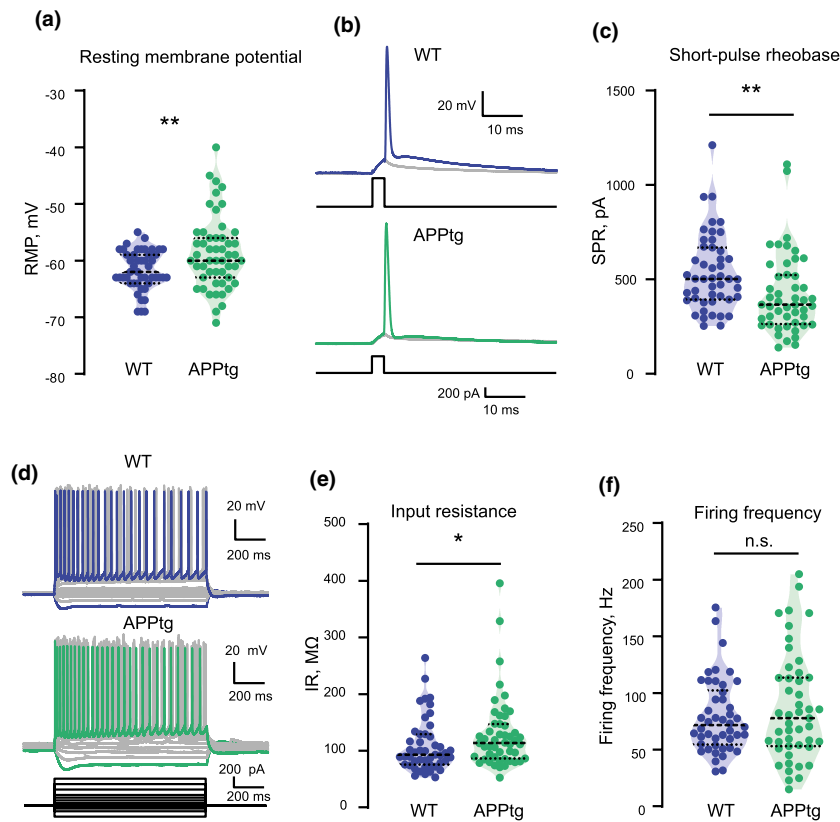


FIGURE 4 Increased intrinsic excitability of CA1 pyramidal neurons in APPtg rats. (a) APPtg neurons were more depolarized to comparison to WT ones. RMP reached -61.70 ± 3.46 in WT rats ($n = 47$) and -58.67 ± 6.42 in WT rats ($n = 50$) and -61.39 in APPtg rats ($n = 51$) (unpaired t -test, $p = .005$) (b) Short-pulse rheobase (SPR) detected by current injections with $+1$ pA increment. Grey traces display the last subthreshold voltage response, and blue and green trace represents the first suprathreshold responses of WT and APPtg, respectively. The injected currents are depicted as black lines on the bottom. (c) SPR was reduced in APPtg ($n = 44$) in comparison to WT ($n = 48$) neurons (Mann–Whitney test, $p = .0015$). (d) Representative examples of CA1 pyramidal neurons firing behavior in WT (blue traces: current injection of -200 and $+500$ pA) and APPtg (green traces: current injection of -200 and $+500$ pA). (e) Input resistance was increased in APPtg rats (Mann–Whitney test, $p = .039$). (f) CA1 pyramidal neurons fired with initial frequency of 71.62 [54.59 ; 102.4] Hz in WT ($n = 46$) and 77.76 [53.08 ; 113.6] APPtg ($n = 47$) rats (Mann–Whitney test, $p = .65$)

support the findings of the whole-cell current-clamp recordings. The action potential duration was prolonged from 0.29 [0.21 ; 0.36] ms in WT rats to 0.31 [0.24 ; 0.38] ms in APPtg rats (Figure 5h). Taken together, our data support the view that increased intrinsic neuronal excitability of CA1 pyramidal neurons is already present at the beginning of extracellular A β -deposition in APPtg rats.

4 | DISCUSSION

Neuronal network dysfunction is thought to contribute to cognitive deficits in AD and under AD-like conditions in mouse models (Palop et al. 2007; Palop & Mucke, 2016). Here we use a transgenic rat model to analyze hippocampal neuronal network function under AD-like conditions. Performing Ca²⁺-imaging in the hippocampus of anesthetized McGill-R-Thy1-APP rats in vivo revealed the presence of hyperactive CA1 neurons indicating changes on the neuronal microcircuit and network level. Although impaired inhibition has been previously shown to contribute to neuronal network dysfunction in mouse models (Schmid et al. 2016; Verret et al. 2012), we did not

detect inhibitory deficits in the measured parameters in the rat model. Instead, we found changes in passive electrical properties and intrinsic excitability that resulted in neuronal hyperexcitability. The changes in passive properties and intrinsic excitability observed in this study suggest that intrinsic mechanisms precede circuit-based mechanisms during the progression of amyloidosis.

4.1 | Disturbance of the hippocampal neuronal network

The hippocampus is a key brain region for learning and memory, early affected in AD (Braak & Braak, 1991; Dickerson & Eichenbaum, 2010). The CA1 subregion of the dorsal hippocampus plays a well-established role in the encoding and consolidation of memory (Buzsáki & Moser, 2013; Dumas et al. 2005; Ji & Maren, 2008). The CA1 region receives axonal input from the medial entorhinal cortex, which is known for its early vulnerability in human AD and animal models of AD (Jucker & Ingram, 1997). In addition, the CA1 region receives input from CA3 as part of the trisynaptic

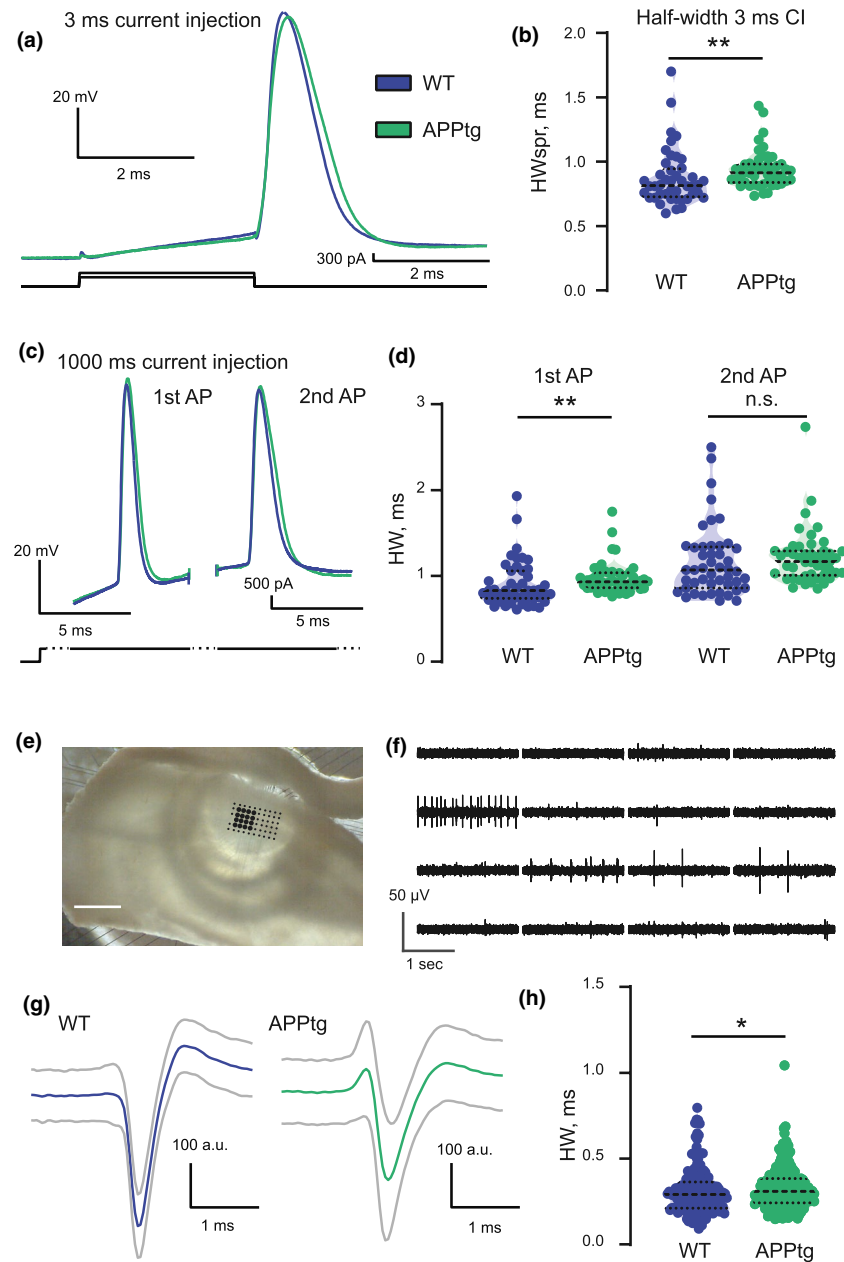


FIGURE 5 Increased action potential duration in APPtg rats. (a) Representative examples of single action potential in WT (blue) and APPtg (green) CA1 pyramidal neurons on the first suprathreshold responses following a 3 ms current injection of 517pA and 352pA, respectively. (b) The half-width of the first suprathreshold action potentials was prolonged in APPtg rats in comparison to WT ($n = 44$ for WT and $n = 48$ for APPtg, Mann-Whitney test, $p = .002$). (c) The first half-width (HW1) and second half-width (HW2) were determined as duration of the first and second action potential at the level of 50% repolarization for a +500 pA step current injection. (d) HW1 was prolonged ($n = 47$ for WT and $n = 51$ for APPtg, Mann-Whitney test, $p = .001$) and was not significantly different for the second action potential (Mann-Whitney test, $p = .087$). (e–h) MEA recordings confirm prolongation of action potential duration in hippocampal slices of APPtg rats. (e) Hippocampal slice on a 6 × 10 electrodes MEA. Scale bar, 1 mm. (f) Original extracellular recordings, corresponding to the eight electrodes, depicted in bold black on the MEA slice image in e. (g) Examples of mean spike waveforms in WT (blue) and APPtg (green) rats. Gray lines correspond to SD values. (h) Distribution of extracellular spike half-widths in WT (199 units in 17 slices, 5 animals) and APPtg (194 units in 21 slices, 9 animals) rats. Extracellular measured action potentials were broadened in APPtg CA1 hippocampal neurons in comparison to WT ones (Mann-Whitney test, $p = .035$)

loop, which has a well-established function in spatial memory processes (Bird & Burgess, 2008). Together with the subiculum, area CA1 shows the earliest progression in A β -plaque load in MCGill APPtg rats (Heggland et al. 2015). One of the emerging tools for understanding of disease related disturbance of cellular and network

function is in vivo two-photon Ca²⁺-imaging. Monitoring neuronal Ca²⁺-transients in the cortex of rats has been previously achieved using head-mounted microscopes (Scott et al. 2018) or by voluntary head restraint in combination with a two-photon microscope (Scott et al. 2013). However, so far two-photon in vivo imaging of deeper



brain structures like the hippocampus has only been reported in mice (Attardo et al. 2015; Dombeck et al. 2010; Gu et al. 2014; Mizrahi et al. 2004). In this study, we now have designed and used a specialized hippocampal cranial window that enabled us to perform hippocampal *in vivo* Ca^{2+} -imaging in the hippocampus of rats. Two-photon imaging of Ca^{2+} -transients in the cortex and hippocampus of mouse models with AD-like pathology has revealed hyperactive neurons in spatial proximity to $\text{A}\beta$ -plaques (Busche et al. 2008). Neuronal hyperactivity was observed both at pre-plaque stages and following $\text{A}\beta$ -plaque deposition (Busche et al. 2012). Using the genetically encoded Ca^{2+} -indicator GCaMP6m, we identified hyperactive neurons in APPTg rats (Figure 2a–i). Compared to the previous experiments performed in mice, overall neuronal activity in the hippocampus was lower. Apart from possible intrinsic hippocampal network properties characteristic for the different model organisms, the reason for this could be the application of a different Ca^{2+} -indicator but also the difference in Ca^{2+} -transient detection. For all models, the observed hyperactivity could be a consequence of a compensatory mechanism in response to reduced input from CA3 or entorhinal cortex. In mice, treatment with a γ -secretase blocker to reduce the amount of $\text{A}\beta$ -generation decreased the number of hyperactive neurons underscoring the importance of $\text{A}\beta$ for neuronal hyperactivity (Busche et al. 2012). Aberrant Ca^{2+} -transient frequency was also detected in the visual cortex of awake mice with AD-like pathology during resting states (Liebscher et al. 2014). Our *in vivo* Ca^{2+} -imaging data confirm these findings and suggest that neuronal hyperactivity is species independent. It is possible, that similar pathomechanisms could be observed in AD patients, which exhibit signs of neuronal hyperactivity in depth recordings of the temporal lobe (Lam et al. 2017). One of the emerging research directions is that neuro-modulation (for review see (Harris et al. 2020)), involving neuronal (Temido-Ferreira et al. 2020; Viana da Silva et al. 2016) and non-neuronal (Delekate et al. 2014) purinergic receptors may be crucially involved in the progress of Alzheimer's pathology. So far, no data are available about changes in purinergic signaling in McGill rat model. This is certainly an important avenue for further investigation.

4.2 | Intact inhibitory parameters at an early stage of $\text{A}\beta$ -plaque deposition

Reduced inhibition represents one of the two current candidate mechanisms for increased neuronal excitability and hyperactivity (Palop et al. 2007; Palop & Mucke, 2016). Impaired parvalbumin-positive (PV^+) GABAergic neurons, a subpopulation of GABAergic neurons involving fast-spiking, soma-targeting basket cells, but also several other cell types (Harris et al. 2018), have been detected in mice with AD-like pathology. Interestingly, specific ectopic expression of Na^+ -channels in PV^+ neurons with the rationale to increase PV interneuron activity was sufficient to improve memory in diseased mice (Verret et al. 2012). Precisely timed optogenetic manipulation of hippocampal PV interneurons improved memory in mice with AD-like pathology (Ambrad Giovannetti et al. 2018)(Etter

et al. 2019). Furthermore, impaired innervation of hippocampal somatostatin-positive GABAergic neurons contributed to reduced formation of post-synaptic spines and learning deficits in mice with AD-like pathology (Schmid et al. 2016). Somatostatin-positive interneurons represent a population of GABAergic neurons comprising several cell types that predominantly targets apical dendrites of pyramidal neurons (Schmid et al. 2016; Verret et al. 2012). Therefore, we tested whether impaired inhibition contributed to the observed hyperactive CA1 neurons in the rat model. Our protocol tested both for proximal and distal recurrent inhibition of CA1 pyramidal neurons in brain slices, as a shift of inhibition from proximal to distal dendritic regions has been reliably observed upon rhythmic and repeated stimulation in the theta and gamma range (Muller et al. 2012; Pouille & Scanziani, 2004; Pouille et al. 2013). Our data revealed intact and unchanged IPSPs at early (more proximal inhibition) and delayed (more distal inhibition) stimulation time points (Figure 3). Our findings suggest that other mechanisms than reduced inhibitory circuit function may underlie the neuronal hyperactivity that is observed in CA1 neurons at the beginning of $\text{A}\beta$ -deposition.

4.3 | Mechanisms of increased excitability

In this study, increased neuronal excitability has been shown for the first time under *in vivo* and *in vitro* experimental conditions in McGill-R-Thy1-APP rats at an early stage of extracellular $\text{A}\beta$ -deposition. We performed experiments both in dorsal (imaging, MEA) and ventral (patch-clamp) hippocampus in agreement with hyperexcitability. Hyperexcitability may have multi-factorial reasons. One line of evidence from *in vitro* studies points to increased extracellular glutamate accumulation because of higher glutamatergic neurotransmission in response to $\text{A}\beta$ aggregates shown by FM1-43 labeling and whole-cell patch-clamp recording (Brito-Moreira et al. 2011; Paula-Lima et al. 2013). Moreover, $\text{A}\beta$ binds to the $\beta 2$ adrenoceptor, which through an intracellular cascade modulates glutamatergic transmission via AMPA receptors (Wang et al. 2010). Additionally, soluble $\text{A}\beta$ increases activation of extrasynaptic NR2B-containing receptors, leading to inhibition of long-term potentiation (Li et al. 2011). Furthermore, suppression of glutamate reuptake may contribute to increased glutamatergic neurotransmission (Zott et al. 2019). However, our *in vivo* findings support an intact glutamatergic neurotransmission in APPTg rats at early stages of $\text{A}\beta$ -plaque deposition (Figure 2j and k).

Another line of evidence follows reduced dendritic arborization, reduced cell size and loss of synapses that have been consistently detected in human AD patients (Adlard & Vickers, 2002; Falke et al. 2003; Grutzendler et al. 2007; Spires & Hyman, 2004) and in animal models (Grutzendler et al. 2007; Le et al. 2001; Moolman et al. 2004; Tsai et al. 2004). Modeling and experimental studies have shown that reduced cell size and membrane area may alter the input–output function of pyramidal cells by increasing the input resistance of neurons (Siskova et al. 2014). Such an increase in input resistance facilitates the firing of action potentials in response to synaptic input (Siskova et al. 2014).

Indeed, APPTg rats exhibited an increased input resistance and reduced short-pulse rheobase at 6–9 months of age (Figure 4). Such electrophysiological changes have not been observed at earlier stages (age 3–4 months) in the same APPTg rat model (Heggland et al. 2019; Qi et al. 2014). In addition, the increased action potential half-width observed in this study further supports the view that intrinsic excitability changes in neurons contribute to neuronal hyperexcitability at early stages. A β may affect large-conductance calcium-activated potassium (BK) channels thereby contributing to the cellular hyperexcitability (Wang et al. 2015). Mechanistically, a broadening of action potentials may facilitate and increase synaptic glutamate release (Deng et al. 2013). Moreover, the synaptic input–output relationships were indistinguishable between 6- and 9-month-old WT and APPTg rats, challenging the hypothesis of increased glutamatergic synaptic transmission.

Our findings suggest that neuronal hyperexcitability at an early stage of extracellular A β deposition is mediated by changes in the intrinsic excitability of CA1 pyramidal neurons, rather than by synaptic changes. Thus, our data support the view that altered intrinsic excitability precedes inhibitory and excitatory synaptic dysfunction during disease progression.

4.4 | Statistical information

Shapiro–Wilco test was performed to test for normality for datasets with $n < 50$, Kolmogorov–Smirnov test was performed to test for normality for datasets with $n > 50$. Unpaired Student's *t*-test analysis (two-tailed), Mann–Whitney test or Kolmogorov–Smirnov test were performed where applicable. In experiments where more conditions were evaluated, one-way or two-way RM ANOVAs were performed followed by multiple comparisons testing using the Sidak's correction method. * $p < .05$, ** $p < .01$, *** $p < .001$. No test for outliers was conducted.

5 | AUTHORS' INFORMATION

Liudmila Sosulina and Manuel Mittag contributed equally to this work. Martin Fuhrmann and Stefan Remy also contributed equally.

6 | COMPETING FINANCIAL INTERESTS

All authors declare no competing financial or other interests.

7 | MATERIAL AND CORRESPONDENCE

Materials are available on request. All correspondence should be directed to Martin Fuhrmann or Stefan Remy.

ACKNOWLEDGMENT

We are grateful for the expert technical assistance of Meltem Eryilmaz.

All experiments were conducted in compliance with the ARRIVE guidelines.

AUTHORS' CONTRIBUTIONS

M.F., S.R., A.C.C., M.R., L.S., and M.M. were involved in the design of the study. A.C.C. participated in initial research planning discussions and the provision of well characterized McGill-R-Thy1-APP transgenic breeders. M.F., S.R., L.S., M.M., and H.-R.G. co-wrote the paper. L.S., Y.Q. and H.-R.G. performed the electrophysiology experiments and analyzed the data and prepared figures. I.K. assisted in designing electrophysiology recordings. M.M. and K.H. conducted the Ca²⁺-imaging. M.M. analyzed the Ca²⁺-imaging data and prepared figures. N.H. did morphological reconstructions. K.K. and F.F. provided microscopy assistance. J.S., D.F. did the histological stainings and prepared figures. D.J. provided data analysis assistance.

DATA AVAILABILITY STATEMENT

The datasets generated during and/or analyzed during this study are available within the article or the supplementary information files or from the corresponding authors upon reasonable request.

ORCID

Manuel Mittag  <https://orcid.org/0000-0001-9908-3464>

REFERENCES

- Adlard, P. A., & Vickers, J. C. (2002). Morphologically distinct plaque types differentially affect dendritic structure and organization in the early and late stages of Alzheimer's disease. *Acta Neuropathologica*, 103, 377–383. <https://doi.org/10.1007/s00401-001-0476-6>
- Ambrad Giovannetti E., & Fuhrmann M. (2019). Unsupervised excitation: GABAergic dysfunctions in Alzheimer's disease. *Brain Research*, 1707, 216–226. <http://dx.doi.org/10.1016/j.brainres.2018.11.042>
- Ambrad Giovannetti, E., Poll, S., Justus, D., Kaneko, H., Fuhrmann, F., Steffen, J., Remy, S., & Fuhrmann, M. (2018). Restoring Memory by Optogenetic Synchronization of Hippocampal Oscillations in an Alzheimer's Disease Mouse Model, *bioRxiv*, 363820. <https://doi.org/10.1101/363820>
- Attardo, A., Fitzgerald, J. E., & Schnitzer, M. J. (2015). Impermanence of dendritic spines in live adult CA1 hippocampus. *Nature*, 523, 592–596. <https://doi.org/10.1038/nature14467>
- Bakker, A., Krauss, G. L., Albert, M. S., Speck, C. L., Jones, L. R., Stark, C. E., Yassa, M. A., Bassett, S. S., Shelton, A. L., & Gallagher, M. (2012). Reduction of hippocampal hyperactivity improves cognition in amnesic mild cognitive impairment. *Neuron*, 74, 467–474. <https://doi.org/10.1016/j.neuron.2012.03.023>
- Bezzina, C., Verret, L., Juan, C., Remaud, J., Halley, H., Rampon, C., & Dahan, L. (2015). Early onset of hypersynchronous network activity and expression of a marker of chronic seizures in the Tg2576 mouse model of Alzheimer's disease. *PLoS One*, 10, e0119910. <https://doi.org/10.1371/journal.pone.0119910>
- Bird, C. M., & Burgess, N. (2008). The hippocampus and memory: Insights from spatial processing. *Nature Reviews. Neuroscience*, 9, 182–194.
- Bittner, T., Burgold, S., Dorostkar, M. M., Fuhrmann, M., Wegenast-Braun, B. M., Schmidt, B., Kretschmar, H., & Herms, J. (2012). Amyloid plaque formation precedes dendritic spine loss. *Acta Neuropathologica*, 124, 797–807. <https://doi.org/10.1007/s00401-012-1047-8>



- Bittner, T., Fuhrmann, M., Burgold, S., Ochs, S. M., Hoffmann, N., Mitteregger, G., Kretschmar, H., LaFerla, F. M., & Herms, J. (2010). Multiple events lead to dendritic spine loss in triple transgenic Alzheimer's disease mice. *PLoS One*, 5, e15477. <https://doi.org/10.1371/journal.pone.0015477>
- Braak, H., & Braak, E. (1991). Demonstration of amyloid deposits and neurofibrillary changes in whole brain sections. *Brain Pathology*, 1, 213–216. <https://doi.org/10.1111/j.1750-3639.1991.tb00661.x>
- Brito-Moreira, J., Paula-Lima, A. C., Bomfim, T. R., Oliveira, F. B., Sepúlveda, F. J., De Mello, F. G., Aguayo, L. G., Panizzutti, R., & Ferreira, S. T. (2011). A β oligomers induce glutamate release from hippocampal neurons. *Current Alzheimer Research*, 8, 552–562.
- Brown, J. T., Chin, J., Leiser, S. C., Pangalos, M. N., & Randall, A. D. (2011). Altered intrinsic neuronal excitability and reduced Na⁺ currents in a mouse model of Alzheimer's disease. *Neurobiology of Aging*, 32(2109), e2101–2114. <https://doi.org/10.1016/j.neurobiolaging.2011.05.025>
- Busche, M. A., Chen, X., Henning, H. A., Reichwald, J., Staufenbiel, M., Sakmann, B., & Konnerth, A. (2012). Critical role of soluble amyloid-beta for early hippocampal hyperactivity in a mouse model of Alzheimer's disease. *Proceedings of the National Academy of Sciences of the United States of America*, 109, 8740–8745.
- Busche, M. A., Eichhoff, G., Adelsberger, H., Abramowski, D., Wiederhold, K. H., Haass, C., Staufenbiel, M., Konnerth, A., & Garaschuk, O. (2008). Clusters of hyperactive neurons near amyloid plaques in a mouse model of Alzheimer's disease. *Science*, 321, 1686–1689. <https://doi.org/10.1126/science.1162844>
- Buzsáki, G., & Moser, E. I. (2013). Memory, navigation and theta rhythm in the hippocampal-entorhinal system. *Nature Neuroscience*, 16, 130–138. <https://doi.org/10.1038/nn.3304>
- Chen, T.-W., Wardill, T. J., Sun, Y. I., Pulver, S. R., Renninger, S. L., Baohan, A., Schreiter, E. R., Kerr, R. A., Orger, M. B., Jayaraman, V., Looger, L. L., Svoboda, K., & Kim, D. S. (2013). Ultrasensitive fluorescent proteins for imaging neuronal activity. *Nature*, 499, 295–300. <https://doi.org/10.1038/nature12354>
- Damas, S., Halley, H., Frances, B., & Lassalle, J. M. (2005). Encoding, consolidation, and retrieval of contextual memory: Differential involvement of dorsal CA3 and CA1 hippocampal subregions. *Learning & Memory (Cold Spring Harbor, N.Y.)*, 12, 375–382.
- Deleate, A., Fuchtemeier, M., Schumacher, T., Ulbrich, C., Foddis, M., & Petzold, G. C. (2014). Metabotropic P2Y₁ receptor signalling mediates astrocytic hyperactivity in vivo in an Alzheimer's disease mouse model. *Nature Communications*, 5, 5422. <https://doi.org/10.1038/ncomms6422>
- Deng, P. Y., Rotman, Z., Blundon, J. A., Cho, Y., Cui, J., Cavalli, V., Zakharenko, S. S., & Klyachko, V. A. (2013). FMRP regulates neurotransmitter release and synaptic information transmission by modulating action potential duration via BK channels. *Neuron*, 77, 696–711. <https://doi.org/10.1016/j.neuron.2012.12.018>
- Dickerson, B. C., & Eichenbaum, H. (2010). The episodic memory system: Neurocircuitry and disorders. *Neuropsychopharmacology: Official Publication of the American College of Neuropsychopharmacology*, 35, 86–104. <https://doi.org/10.1038/npp.2009.126>
- Dombeck, D. A., Harvey, C. D., Tian, L., Looger, L. L., & Tank, D. W. (2010). Functional imaging of hippocampal place cells at cellular resolution during virtual navigation. *Nature Neuroscience*, 13, 1433–1440. <https://doi.org/10.1038/nn.2648>
- Etter, G., van der Veldt, S., Manseau, F., Zarrinkoub, I., Trillaud-Doppia, E., & Williams, S. (2019). Optogenetic gamma stimulation rescues memory impairments in an Alzheimer's disease mouse model. *Nature Communications*, 10, 5322. <https://doi.org/10.1038/s41467-019-13260-9>
- Falke, E., Nissarov, J., Mitchell, T. W., Bennett, D. A., Trojanowski, J. Q., & Arnold, S. E. (2003). Subicular dendritic arborization in Alzheimer's disease correlates with neurofibrillary tangle density. *American Journal of Pathology*, 163, 1615–1621. [https://doi.org/10.1016/S0002-9440\(10\)63518-3](https://doi.org/10.1016/S0002-9440(10)63518-3)
- Fuhrmann, F., Justus, D., Sosulina, L., Kaneko, H., Beutel, T., Friedrichs, D., Schoch, S., Schwarz, M. K., Fuhrmann, M., & Remy, S. (2015). Locomotion, theta oscillations, and the speed-correlated firing of hippocampal neurons are controlled by a medial septal glutamatergic circuit. *Neuron*, 86, 1253–1264. <https://doi.org/10.1016/j.neuron.2015.05.001>
- Galeano, P., Martino Adami, P. V., Do Carmo, S., Blanco, E., Rotondaro, C., Capani, F., Castano, E. M., Cuello, A. C., & Morelli, L. (2014). Longitudinal analysis of the behavioral phenotype in a novel transgenic rat model of early stages of Alzheimer's disease. *Frontiers in Behavioral Neurosciences*, 8, 321. <https://doi.org/10.3389/fnbeh.2014.00321>
- Grutzendler, J., Helmin, K., Tsai, J., & Gan, W. B. (2007). Various dendritic abnormalities are associated with fibrillar amyloid deposits in Alzheimer's disease. *Annals of the New York Academy of Sciences*, 1097, 30–39. <https://doi.org/10.1196/annals.1379.003>
- Gu, L., Kleiber, S., Schmid, L., Nebeling, F., Chamoun, M., Steffen, J., Wagner, J., & Fuhrmann, M. (2014). Long-term in vivo imaging of dendritic spines in the hippocampus reveals structural plasticity. *Journal of Neuroscience*, 34, 13948–13953. <https://doi.org/10.1523/JNEUROSCI.1464-14.2014>
- Hamm, V., Heraud, C., Bott, J. B., Herbeaux, K., Strittmatter, C., Mathis, C., & Goutagny, R. (2017). Differential contribution of APP metabolites to early cognitive deficits in a TgCRND8 mouse model of Alzheimer's disease. *Science Advances*, 3, e1601068. <https://doi.org/10.1126/sciadv.1601068>
- Harris, K. D., Hochgerner, H., Skene, N. G., Magno, L., Katona, L., Bengtsson Gonzales, C., Somogyi, P., Kessaris, N., Linnarsson, S., & Hjerling-Leffler, J. (2018). Classes and continua of hippocampal CA1 inhibitory neurons revealed by single-cell transcriptomics. *PLoS Biology*, 16, e2006387. <https://doi.org/10.1371/journal.pbio.2006387>
- Harris, S. S., Wolf, F., De Strooper, B., & Busche, M. A. (2020). Tipping the scales: Peptide-dependent dysregulation of neural circuit dynamics in Alzheimer's disease. *Neuron*, 107, 417–435. <https://doi.org/10.1016/j.neuron.2020.06.005>
- Heggland I., Kvello P., & Witter M. P. (2019). Electrophysiological characterization of networks and single cells in the hippocampal region of a transgenic rat model of Alzheimer's disease. *eneuro*, 6, 1–16. <http://dx.doi.org/10.1523/eneuro.0448-17.2019>
- Heggland, I., Storkaas, I. S., Soligard, H. T., Kibro-Flatmoen, A., & Witter, M. P. (2015). Stereological estimation of neuron number and plaque load in the hippocampal region of a transgenic rat model of Alzheimer's disease. *European Journal of Neuroscience*, 41, 1245–1262. <https://doi.org/10.1111/ejn.12876>
- Hollnagel, J. O., Elzoheiry, S., Gorgas, K., Kins, S., Beretta, C. A., Kirsch, J., Kuhse, J., Kann, O., & Kiss, E. (2019). Early alterations in hippocampal perisomatic GABAergic synapses and network oscillations in a mouse model of Alzheimer's disease amyloidosis. *PLoS One*, 14, e0209228. <https://doi.org/10.1371/journal.pone.0209228>
- Iaccarino, H. F., Singer, A. C., Martorell, A. J., Rudenko, A., Gao, F., Gillingham, T. Z., Mathys, H., Seo, J., Kritskiy, O., Abdurrob, F., Adaikkan, C., Canter, R. G., Rueda, R., Brown, E. N., Boyden, E. S., & Tsai, L.-H. (2016). Gamma frequency entrainment attenuates amyloid load and modifies microglia. *Nature*, 540, 230–235. <https://doi.org/10.1038/nature20587>
- Ittner, A. A., Gladbach, A., Bertz, J., Suh, L. S., & Ittner, L. M. (2014). p38 MAP kinase-mediated NMDA receptor-dependent suppression of hippocampal hypersynchronicity in a mouse model of Alzheimer's disease. *Acta Neuropathologica Communications*, 2, 149. <https://doi.org/10.1186/s40478-014-0149-z>
- Ji, J., & Maren, S. (2008). Differential roles for hippocampal areas CA1 and CA3 in the contextual encoding and retrieval of extinguished fear. *Learning & Memory (Cold Spring Harbor N.Y.)*, 15, 244–251.

- Jucker, M., & Ingram, D. K. (1997). Murine models of brain aging and age-related neurodegenerative diseases. *Behavioural Brain Research*, 85, 1–26. [https://doi.org/10.1016/S0166-4328\(96\)02243-7](https://doi.org/10.1016/S0166-4328(96)02243-7)
- Kazim, S. F., Chuang, S. C., Zhao, W., Wong, R. K., Bianchi, R., & Iqbal, K. (2017). Early-onset network hyperexcitability in presymptomatic Alzheimer's disease transgenic mice is suppressed by passive immunization with anti-human APP/Abeta antibody and by mGluR5 blockade. *Frontiers in Aging Neuroscience*, 9, 71.
- Lam, A. D., Deck, G., Goldman, A., Eskandar, E. N., Noebels, J., & Cole, A. J. (2017). Silent hippocampal seizures and spikes identified by foramen ovale electrodes in Alzheimer's disease. *Nature Medicine*, 23, 678–680. <https://doi.org/10.1038/nm.4330>
- Le, R., Cruz, L., Urbanc, B., Knowles, R. B., Hsiao-Ashe, K., Duff, K., Irizarry, M. C., Stanley, H. E., & Hyman, B. T. (2001). Plaque-induced abnormalities in neurite geometry in transgenic models of Alzheimer disease: Implications for neural system disruption. *Journal of Neuropathology and Experimental Neurology*, 60, 753–758. <https://doi.org/10.1093/jnen/60.8.753>
- Leon, W. C., Canneva, F., Partridge, V. et al (2010). A novel transgenic rat model with a full Alzheimer's-like amyloid pathology displays pre-plaque intracellular amyloid-beta-associated cognitive impairment. *Journal of Alzheimer's Disease: JAD*, 20, 113–126.
- Li, S., Jin, M., Koeglspenger, T., Shepardon, N. E., Shankar, G. M., & Selkoe, D. J. (2011). Soluble A β oligomers inhibit long-term potentiation through a mechanism involving excessive activation of extrasynaptic NR2B-containing NMDA receptors. *Journal of Neuroscience*, 31, 6627–6638.
- Liebscher, S., Page, R. M., Kafer, K. et al (2014). Chronic gamma-secretase inhibition reduces amyloid plaque-associated instability of pre- and postsynaptic structures. *Molecular Psychiatry*, 19, 937–946.
- Magee, J. C., & Cook, E. P. (2000). Somatic EPSP amplitude is independent of synapse location in hippocampal pyramidal neurons. *Nature Neuroscience*, 3, 895–903. <https://doi.org/10.1038/78800>
- Maier, N., Morris, G., Jochenning, F. W., & Schmitz, D. (2009). An approach for reliably investigating hippocampal sharp wave-ripples In Vitro. *PLoS One*, 4, e6925. <https://doi.org/10.1371/journal.pone.0006925>
- Minkeviciene, R., Rheims, S., Dobszay, M. B. et al (2009). Amyloid beta-induced neuronal hyperexcitability triggers progressive epilepsy. *Journal of Neuroscience*, 29, 3453–3462.
- Mizrahi, A., Crowley, J. C., Shtoyerman, E., & Katz, L. C. (2004). High-resolution in vivo imaging of hippocampal dendrites and spines. *Journal of Neuroscience*, 24, 3147–3151. <https://doi.org/10.1523/JNEUROSCI.5218-03.2004>
- Moolman, D. L., Vitolo, O. V., Vonsattel, J. P., & Shelanski, M. L. (2004). Dendrite and dendritic spine alterations in Alzheimer models. *Journal of Neurocytology*, 33, 377–387. <https://doi.org/10.1023/B:NEUR.0000044197.83514.64>
- Mucke, L., & Selkoe, D. J. (2012). Neurotoxicity of amyloid beta-protein: Synaptic and network dysfunction. *Cold Spring Harbor Perspectives in Medicine*, 2, a006338.
- Muller, C., Beck, H., Coulter, D., & Remy, S. (2012). Inhibitory control of linear and supralinear dendritic excitation in CA1 pyramidal neurons. *Neuron*, 75, 851–864. <https://doi.org/10.1016/j.neuron.2012.06.025>
- Palop, J. J., Chin, J., Roberson, E. D., Wang, J., Thwin, M. T., Bien-Ly, N., Yoo, J., Ho, K. O., Yu, G.-Q., Kreitzer, A., Finkbeiner, S., Noebels, J. L., & Mucke, L. (2007). Aberrant excitatory neuronal activity and compensatory remodeling of inhibitory hippocampal circuits in mouse models of Alzheimer's disease. *Neuron*, 55, 697–711. <https://doi.org/10.1016/j.neuron.2007.07.025>
- Palop, J. J., & Mucke, L. (2016). Network abnormalities and interneuron dysfunction in Alzheimer disease. *Nature Reviews. Neuroscience*, 17, 777–792.
- Paula-Lima, A. C., Brito-Moreira, J., & Ferreira, S. T. (2013). Deregulation of excitatory neurotransmission underlying synapse failure in Alzheimer's disease. *Journal of Neurochemistry*, 126, 191–202. <https://doi.org/10.1111/jnc.12304>
- Petrasek, T., Vojtechova, I., Lobellova, V., Popelikova, A., Janikova, M., Brozka, H., Houdek, P., Sladek, M., Sumova, A., Kristofikova, Z., Vales, K., & Stuchlik, A. (2018). The McGill transgenic rat model of Alzheimer's disease displays cognitive and motor impairments, changes in anxiety and social behavior, and altered circadian activity. *Frontiers in Aging Neuroscience*, 10, 250–250. <https://doi.org/10.3389/fnagi.2018.00250>
- Pouille, F., & Scanziani, M. (2004). Routing of spike series by dynamic circuits in the hippocampus. *Nature*, 429, 717–723. <https://doi.org/10.1038/nature02615>
- Pouille, F., Watkinson, O., Scanziani, M., & Trevelyan, A. J. (2013). The contribution of synaptic location to inhibitory gain control in pyramidal cells. *Physiological Reports*, 1, e00067. <https://doi.org/10.1002/phy2.67>
- Qi, Y., Klyubin, I., Harney, S. C. et al (2014). Longitudinal testing of hippocampal plasticity reveals the onset and maintenance of endogenous human Abeta-induced synaptic dysfunction in individual freely behaving pre-plaque transgenic rats: Rapid reversal by anti-Abeta agents. *Acta Neuropathologica Communications*, 2, 175.
- Rossant, C., Kadir, S. N., Goodman, D. F. M., Schulman, J., Hunter, M. L. D., Saleem, A. B., Grosmark, A., Belluscio, M., Denfield, G. H., Ecker, A. S., Tolias, A. S., Solomon, S., Buzsáki, G., Carandini, M., & Harris, K. D. (2016). Spike sorting for large, dense electrode arrays. *Nature Neuroscience*, 19, 634–641. <https://doi.org/10.1038/nn.4268>
- Rowan, M. J., Klyubin, I., Cullen, W. K., & Anwyl, R. (2003). Synaptic plasticity in animal models of early Alzheimer's disease. *Philosophical Transactions of the Royal Society of London. Series B, Biological Sciences*, 358, 821–828. <https://doi.org/10.1098/rstb.2002.1240>
- Sanchez, P. E., Zhu, L., Verret, L., Vossel, K. A., Orr, A. G., Cirrito, J. R., Devidze, N., Ho, K., Yu, G.-Q., Palop, J. J., & Mucke, L. (2012). Levetiracetam suppresses neuronal network dysfunction and reverses synaptic and cognitive deficits in an Alzheimer's disease model. *Proceedings of the National Academy of Sciences of the United States of America*, 109, E2895–2903. <https://doi.org/10.1073/pnas.1121081109>
- Schmid, L. C., Mittag, M., Poll, S., Steffen, J., Wagner, J., Geis, H.-R., Schwarz, I., Schmidt, B., Schwarz, M. K., Remy, S., & Fuhrmann, M. (2016). Dysfunction of somatostatin-positive interneurons associated with memory deficits in an Alzheimer's disease model. *Neuron*, 92, 114–125. <https://doi.org/10.1016/j.neuron.2016.08.034>
- Scott, B. B., Brody, C. D., & Tank, D. W. (2013). Cellular resolution functional imaging in behaving rats using voluntary head restraint. *Neuron*, 80, 371–384. <https://doi.org/10.1016/j.neuron.2013.08.002>
- Scott, B. B., Thiberge, S. Y., Guo, C., Tervo, D. G. R., Brody, C. D., Karpova, A. Y., & Tank, D. W. (2018). Imaging cortical dynamics in GCaMP transgenic rats with a head-mounted widefield microscope. *Neuron*, 100(1045–1058), e1045. <https://doi.org/10.1016/j.neuron.2018.09.050>
- Šišková, Z., Justus, D., Kaneko, H., Friedrichs, D., Henneberg, N., Beutel, T., Pitsch, J., Schoch, S., Becker, A., von der Kammer, H., & Remy, S. (2014). Dendritic structural degeneration is functionally linked to cellular hyperexcitability in a mouse model of Alzheimer's disease. *Neuron*, 84, 1023–1033. <https://doi.org/10.1016/j.neuron.2014.10.024>
- Siwek, M. E., Müller, R., Henseler, C., Trog, A., Lundt, A., Wormuth, C., Broich, K., Ehninger, D., Weiergräber, M., & Papazoglou, A. (2015). Altered theta oscillations and aberrant cortical excitatory activity in the 5XFAD model of Alzheimer's disease. *Neural Plasticity*, 2015, 781731. <https://doi.org/10.1155/2015/781731>
- Spires, T. L., & Hyman, B. T. (2004). Neuronal structure is altered by amyloid plaques. *Reviews in the Neurosciences*, 15, 267–278. <https://doi.org/10.1515/REVNEURO.2004.15.4.267>
- Stringer, C., Pachitariu, M., Steinmetz, N. A., Okun, M., Bartho, P., Harris, K. D., Sahani, M., & Lesica, N. A. (2016). Inhibitory control



- of correlated intrinsic variability in cortical networks. *Elife*, 5, 1–33. <https://doi.org/10.7554/eLife.19695>
- Temido-Ferreira, M., Ferreira, D. G., Batalha, V. L., Marques-Morgado, I., Coelho, J. E., Pereira, P., Gomes, R., Pinto, A., Carvalho, S., Canas, P. M., Cuvelier, L., Buée-Scherrer, V., Faivre, E., Baqi, Y., Müller, C. E., Pimentel, J., Schiffmann, S. N., Buée, L., Bader, M., ... Lopes, L. V. (2020). Age-related shift in LTD is dependent on neuronal adenosine A(2A) receptors interplay with mGluR5 and NMDA receptors. *Molecular Psychiatry*, 25, 1876–1900. <https://doi.org/10.1038/s41380-018-0110-9>
- Tsai, J., Grutzendler, J., Duff, K., & Gan, W. B. (2004). Fibrillar amyloid deposition leads to local synaptic abnormalities and breakage of neuronal branches. *Nature Neuroscience*, 7, 1181–1183. <https://doi.org/10.1038/nn1335>
- Verret, L., Mann, E. O., Hang, G. B., Barth, A. M. I., Cobos, I., Ho, K., Devidze, N., Masliah, E., Kreitzer, A. C., Mody, I., Mucke, L., & Palop, J. J. (2012). Inhibitory interneuron deficit links altered network activity and cognitive dysfunction in Alzheimer model. *Cell*, 149, 708–721. <https://doi.org/10.1016/j.cell.2012.02.046>
- Viana da Silva, S., Haberl, M. G., Zhang, P., Bethge, P., Lemos, C., Gonçalves, N., Gorlewicz, A., Malezieux, M., Gonçalves, F. Q., Grosjean, N., Blanchet, C., Frick, A., Nägerl, U. V., Cunha, R. A., & Mulle, C. (2016). Early synaptic deficits in the APP/PS1 mouse model of Alzheimer's disease involve neuronal adenosine A2A receptors. *Nature Communications*, 7, 11915. <https://doi.org/10.1038/ncomms11915>
- Wang, D., Govindaiah, G., Liu, R., De Arcangelis, V., Cox, C. L., & Xiang, Y. K. (2010). Binding of amyloid beta peptide to beta2 adrenergic receptor induces PKA-dependent AMPA receptor hyperactivity. *The FASEB Journal*, 24, 3511–3521.
- Wang, L., Kang, H., Li, Y., Shui, Y., Yamamoto, R., Sugai, T., & Kato, N. (2015). Cognitive recovery by chronic activation of the large-conductance calcium-activated potassium channel in a mouse model of Alzheimer's disease. *Neuropharmacology*, 92, 8–15. <https://doi.org/10.1016/j.neuropharm.2014.12.033>
- Wilson, E. N., Abela, A. R., Do Carmo, S., Allard, S., Marks, A. R., Welikovitsh, L. A., Ducatzenzeiler, A., Chudasama, Y., & Cuello, A. C. (2017). Intraneuronal amyloid beta accumulation disrupts hippocampal CRTC1-dependent gene expression and cognitive function in a rat model of Alzheimer disease. *Cerebral Cortex (New York, N.Y.: 1991)* 27, 1501–1511.
- Zott, B., Simon, M. M., Hong, W., Unger, F., Chen-Engerer, H.-J., Frosch, M. P., Sakmann, B., Walsh, D. M., & Konnerth, A. (2019). A vicious cycle of β amyloid-dependent neuronal hyperactivation. *Science*, 365, 559–565. <https://doi.org/10.1126/science.aay0198>

SUPPORTING INFORMATION

Additional supporting information may be found online in the Supporting Information section.

How to cite this article: Sosulina L, Mittag M, Geis H-R, et al. Hippocampal hyperactivity in a rat model of Alzheimer's disease. *J Neurochem*. 2021;157:2128–2144. <https://doi.org/10.1111/jnc.15323>